

1 **A vorticity-divergence view of internal wave generation**
2 **by tropical cyclones: insights from Super Typhoon**
3 **Mangkhut**

4 **Noel G. Brizuela¹, T. M. Shaun Johnston¹, Matthew H. Alford¹, Olivier**
5 **Asselin¹, Daniel L. Rudnick¹, James N. Moum², Elizabeth J. Thompson³,**
6 **Shuguang Wang⁴, Chia-Ying Lee⁵**

7 ¹Scripps Institution of Oceanography, University of California, San Diego, La Jolla, CA, USA

8 ²College of Earth, Ocean and Atmospheric Science, Oregon State University, Corvallis, OR, USA

9 ³NOAA Physical Sciences Laboratory, Boulder, CO, USA

10 ⁴Department of Applied Physics and Applied Mathematics, Columbia University, New York, NY, USA

11 ⁵Lamont-Doherty Earth Observatory, Columbia University, New York, NY, USA

12 **Key Points:**

- 13 • Internal wave generation by a Super Typhoon explained using float data, linear
14 theory and a 3D model
- 15 • Coupling between ocean vorticity and divergence relates wind forcing to thermo-
16 cline motions
- 17 • Data suggest spatiotemporal modulation of turbulence by the phase of internal
18 waves in typhoon wakes

Corresponding author: Noel G. Brizuela, nogutier@ucsd.edu

Abstract

Tropical cyclones (TCs) are powered by heat fluxes across the air-sea interface, which are in turn influenced by subsurface physical processes that can modulate storm intensity. Here, we use data from 6 profiling floats to recreate 3D fields of temperature (T), salinity (S), and velocity (u, v, w) around Super Typhoon Mangkhut (western North Pacific, September 2018). Vertical profiles of T and S show the gradual mixing of rainfall and thermocline waters into the mixed layer with diffusivities as high as $\kappa \sim 10^{-1} \text{ m}^2 \text{ s}^{-1}$, causing an asymmetric cold wake of sea surface temperature (SST). A linear model is used to explain observational estimates of vorticity $\zeta = \frac{\partial v}{\partial x} - \frac{\partial u}{\partial y}$, divergence $\Gamma = \frac{\partial u}{\partial x} + \frac{\partial v}{\partial y}$, and their relation to w as coupling between ζ and Γ gives rise to near-inertial waves (NIWs) in the TC wake. Output from a 3D coupled model helps verify observations and an explicit, linear statement of inertial pumping derived in Section 3. Lastly, we find evidence that narrow streaks of enhanced κ aligned with the phase of mode-1 internal waves as they propagated away from the storm track. These analyses provide an observational summary of the ocean response to TCs, demonstrate the advantages of ζ and Γ for the study of internal wave fields, and provide conceptual clarity on the mechanisms that lead to NIW generation behind TCs.

Plain Language Summary

Near-inertial internal waves (NIWs) are periodic fluctuations in the internal structure of ocean currents and stratification. Turbulence induced by the vertical shear in these waves is key to sustain the upper ocean stratification and circulation. In this study, we use data from 6 autonomous floats deployed ahead of Super Typhoon Mangkhut to reconstruct the 3D ocean response to it. Reconstructed velocity fields agree with output from a coupled 3D model. Linear equations for vorticity and divergence are used to explain patterns in measured currents and NIW generation, as inertial coupling between wind-driven vorticity and divergence pumps the stratified ocean interior. Measurements of temperature and salinity detail how rainfall and thermocline waters were mixed into the upper ocean by turbulence. Our analyses indicate that turbulent mixing rates are greatest within 100 km of the typhoon eye but remain elevated for at least 600 km behind it.

1 Introduction

Wind-powered currents that rotate near the inertial frequency (f) dominate upper ocean dynamics behind most tropical cyclones (TCs). On the right (left) side of Northern (Southern) hemisphere storms, transient winds amplify the magnitude of inertial currents, but suppress them on the opposite side (Chang & Anthes, 1978; Price, 1981). Horizontal convergence and divergence associated with these currents lead to inertial pumping of the mixed layer (ML) base. This process transfers ML momentum into near-inertial internal waves (NIWs) that later propagate downwards across the ML base and thermocline (Price, 1983; Gill, 1984; D’Asaro et al., 2007; Sanford et al., 2011; Johnston et al., 2021).

Turbulence and advection associated with near-inertial ML oscillations and NIWs help redistribute heat across subsurface reservoirs. This cools the sea surface temperature (SST) during and shortly after TC passage, limiting fluxes of heat to the atmosphere and helping modulate storm intensity (K. A. Emanuel, 1999; Glenn et al., 2016). Net changes in SST induced by TCs are often dominated by mixing but depend on a combination of factors including storm intensity, translation speed (U_{storm}), and preceding ocean conditions (Chang & Anthes, 1978; Vincent et al., 2012; Balaguru et al., 2012; Rudzin et al., 2019). Therefore, the mechanisms of air-sea coupling under TCs must be assessed on a regional and storm-by-storm basis (S. Chen et al., 2017).

68 In this article, we use data from six profiling floats (Johnston et al., 2020) to re-
 69 construct the 3D fields of temperature (T), salinity (S), and currents (u, v, w) beneath
 70 Super Typhoon Mangkhut (Fig. 1). Our treatment of the data is validated using out-
 71 put from a coupled 3D ocean-atmosphere model of Mangkhut and verifying dynamical
 72 connections between multiple reconstructed fields. Under the assumption that the up-
 73 per ocean response to TC forcing approaches a steady state when viewed in storm-following
 74 coordinates (Geisler, 1970), we diagnose the roles of upwelling, advection, and mixing
 75 in the redistribution of subsurface heat and rainfall inputs. Float velocity data are used
 76 to validate linear theory results showing that upwelling and NIW generation under TCs
 77 result from the coupling of ML vorticity (ζ) and divergence (Γ) by Earth’s rotation.

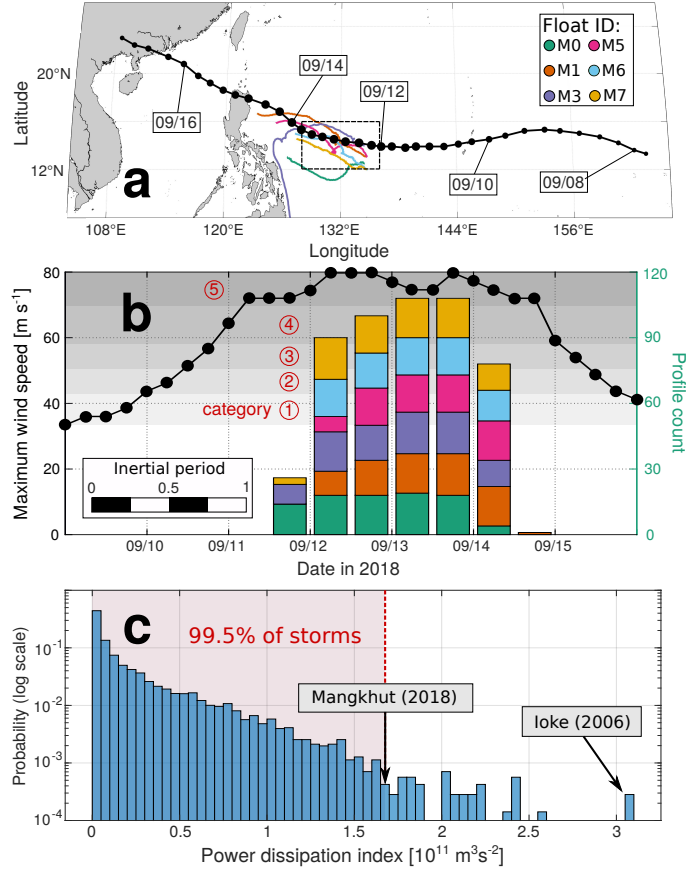


Figure 1. TC overview. (a) shows Joint Typhoon Warning Center best track data for Mangkhut. (b) shows the maximum 1-minute sustained wind speed $|U_{10}|$ (dotted line, left axis). The histogram in b (right axis) shows the time distribution of float measurements used in this study. Gray shading shows the wind speed thresholds for Saffir-Simpson TC categories 1 ($|U_{10}| \leq 30 \text{ m s}^{-1}$) to 5 ($|U_{10}| > 70 \text{ m s}^{-1}$). Estimates of power dissipation index for ≈ 7000 storms place Mangkhut among the 0.5% most powerful tropical storms in record (c).

78 Section 2 describes our data and processing methods including details about the
 79 3D model used for validation. Section 3 lays out the linear theory of upwelling and NIW
 80 generation under TCs and reformulates standard ML dynamics in terms of ζ and Γ to
 81 demonstrate their inertial coupling. Section 4 presents observational and modelled maps
 82 of (u, v) to verify relations between wind forcing, (ζ, Γ) , and NIW generation. The spa-
 83 tiotemporal evolution of T and S under Mangkhut and the role of mixing are described

84 in Section 5. A discussion of our methods and results is presented in Section 6, while con-
 85 clusions are given in Section 7.

86 2 Data and Methods

87 Super Typhoon Mangkhut originated on September 7, 2018 as a tropical depres-
 88 sion in the central Pacific Ocean and later intensified as it moved westwards into the Philip-
 89 pine Sea. Between September 11 and 15, it sustained maximum 1-minute wind speeds
 90 above 70 m s^{-1} , equivalent to a category 5 hurricane. Throughout this period, SOLO-
 91 II floats sampled the ocean response under the TC (Fig. 1b). The combination of Mangkhut’s
 92 long lifespan and elevated intensity put it among the 0.5% most powerful tropical storms
 93 on record (Fig. 1c, K. Emanuel 2005). As it travelled through the Philippine and South
 94 China Seas, Mangkhut caused significant damage and loss of life in the Philippines, Guam,
 95 Taiwan, Hong Kong, and China (Wamsley, 2018).

96 Upon deployment, SOLO-II floats R. Davis et al. (2001) modified their buoyancy
 97 to dive beyond 180 m depth and back to the surface at intervals ranging from 35 to 50
 98 minutes. While doing so, they obtained profiles of T and S , and drifted with the North-
 99 Equatorial Current with a mean zonal velocity $\sim -0.18 \text{ m s}^{-1}$ (Fig. 2a, Johnston et al.
 100 2020). Because floats record their coordinates at the beginning and end of every dive cy-
 101 cle, their Global Positioning System data allows to produce two estimates of horizon-
 102 tal velocity (Fig. 2b). Estimates \mathbf{u}_{mean} are the depth-mean current over the profiling
 103 range and are calculated using the difference between the start and end locations of in-
 104 dividual dives. Surface estimates \mathbf{u}_{surf} , which are subject to wave motion and windage,
 105 are calculated using the drift between consecutive dives, when floats remain at the sur-
 106 face for ~ 5 minutes while they transfer data via Iridium.

107 Output from a coupled ocean-atmosphere model of Mangkhut is used to verify dy-
 108 namical insights derived from float velocity data. The coupled system uses the Weather
 109 Research and Forecast (WRF) model V3.8.1 (Skamarock et al., 2008) as its atmospheric
 110 component, while the ocean is represented by the Hybrid Coordinate Ocean Model V2.2
 111 (HYCOM; Wallcraft et al. 2009). Horizontal grid spacing in HYCOM was $1/12^\circ$ for 41
 112 vertical layers (10 in the upper 50 m) and output was saved at 3 hour intervals. S. S. Chen
 113 & Curcic (2016) give an assessment of this coupled model’s performance under North
 114 Atlantic TCs. Further details about the model configuration used for Mangkhut were
 115 given by Johnston et al. (2021), who first published output from the simulations used
 116 here.

117 Comparisons of model output against measured \mathbf{u}_{surf} (Fig. 3) are indicative of both
 118 the accuracy of the simulation and that of float velocity estimates. Although qualita-
 119 tive agreement between both datasets is good, neither float nor model data in Fig. 3 should
 120 be regarded as ground truth for ocean conditions at a time and place. While \mathbf{u}_{surf} may
 121 be biased by windage or wave motion, the model’s atmospheric component lets Mangkhut
 122 evolve dynamically, such that the modelled track and intensity differ slightly from ob-
 123 servations (Johnston et al., 2021). As described next, objective mapping of float data
 124 onto storm-following coordinates helps make more significant analyses than pointwise
 125 comparisons in Fig. 3.

126 2.1 3D reconstruction of the ocean response

127 Best track data for Mangkhut from the Joint Typhoon Warning Center (JTWC)
 128 was linearly interpolated to the times of float data, which were then reorganized in storm-
 129 following coordinates (x, y) (Fig. 2b). Positive values of x denote regions behind the storm
 130 eye, while $y > 0$ indicates locations right of the TC track. Likewise, \mathbf{u}_{surf} and \mathbf{u}_{mean}
 131 were rotated such that u and v represent along-track and cross-track velocities respec-

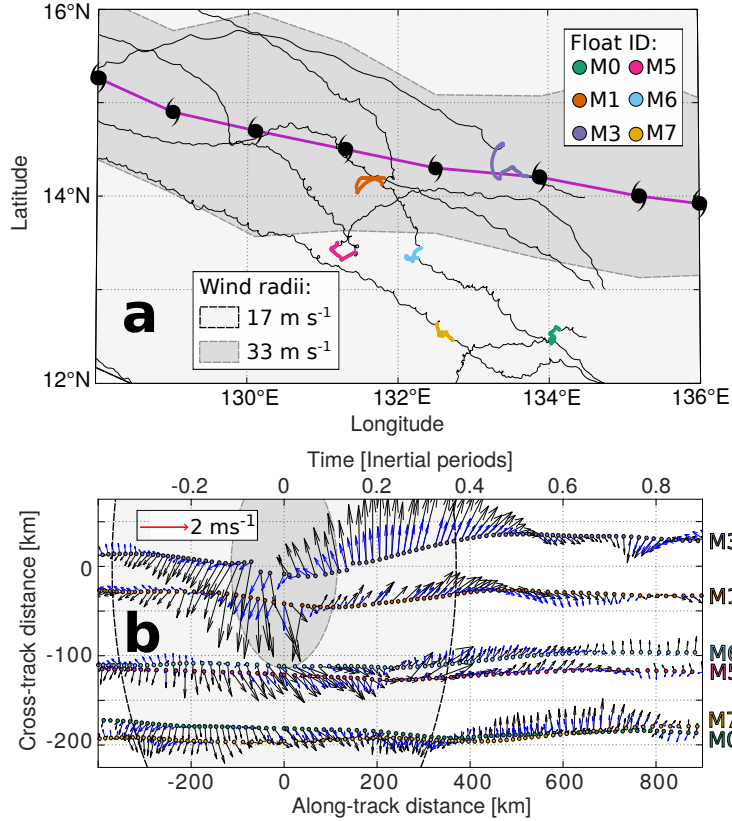


Figure 2. (a) shows 6-hourly JTWC best track data for Mangkhut (purple). Black lines mark the trajectories of SOLO-II floats, while the locations of vertical profiles used in this study are highlighted in colors. (b) shows \mathbf{u}_{surf} (black) and \mathbf{u}_{mean} (blue) in storm-following coordinates (x, y) . Unlike the (x, y) plane, velocity components (u, v) are scaled equally to show the true direction of currents.

132 tively. Plots in (x, y) use the equivalent time $t = x/U_{storm}$ ($U_{storm} = 6.2 \text{ m s}^{-1}$) to
 133 preserve information about temporal variability that has been mapped onto x . Time is
 134 scaled in terms of inertial periods as $t \frac{f}{2\pi}$ using f at 15.54°N . Consequently, one inertial
 135 period in t corresponds to $U_{storm} \frac{2\pi}{f} = 1000 \text{ km}$ in x (Fig. 2b).

136 Despite the fact that each float effectively sampled different parts of the storm at
 137 different times (Fig. 2a), both \mathbf{u}_{surf} and \mathbf{u}_{mean} line up to form a large coherent vortex
 138 around the TC eye (Fig. 2b). This suggests steadiness in the ocean response within the
 139 (x, y) coordinates (Geisler, 1970). To best exploit the spatiotemporal information em-
 140 bedded in float data, we used objective mapping (R. E. Davis, 1985; Le Traon et al., 1998)
 141 with a Gaussian decorrelation scale of 150 km to horizontally interpolate measurements
 142 \mathbf{u}_{surf} , \mathbf{u}_{mean} , T , and S . The signal-to-noise ratio for objective mapping was set to 10,
 143 and areas where the estimated mean square error of interpolated fields is greater than
 144 7.5% of signal variance have been masked out in plots.

145 To reconstruct 3D patterns in T and S , we stacked 2D maps at 5 meter intervals
 146 and produced the 3D fields $T^*(x, y, z)$ and $S^*(x, y, z)$. Here, the star * denotes objec-
 147 tively mapped variables. Although vertical variations in u, v were not measured directly,
 148 we use differences between \mathbf{u}_{surf}^* and \mathbf{u}_{mean}^* to separate the ML flow from the less en-

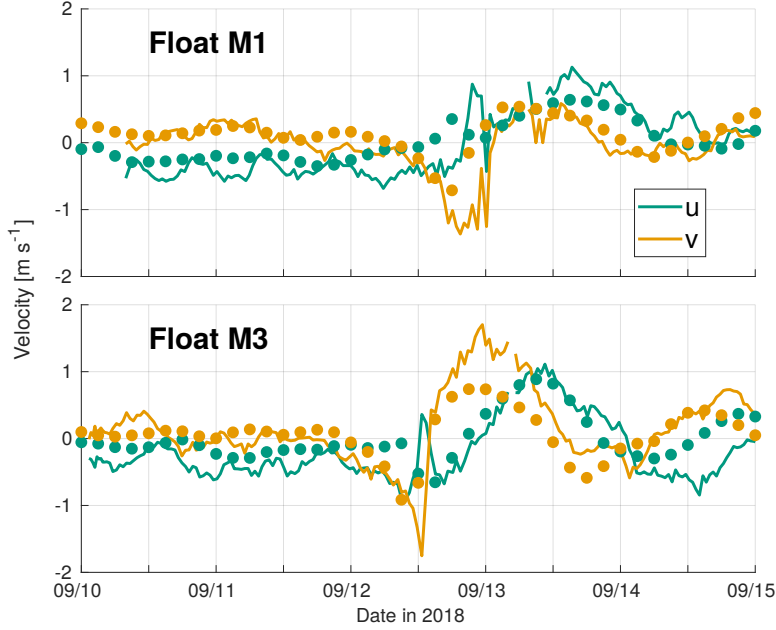


Figure 3. (a) and (b) compare measurements \mathbf{u}_{surf} by floats M1 and M3 (lines) to ML velocity data from a coupled 3D model (circles). Model data was taken from grid cells at the mean location of each float’s measurements within the observation period (Figs. 1b, 2a).

149 ergetic ocean below. More precisely, we assume that depth-dependence at each location
 150 (x, y) is given by

$$151 \quad \mathbf{u}^*(x, y, z) = \begin{cases} \mathbf{u}_{surf}^* & z \geq -h \\ \mathbf{u}_{surf}^* + \left\langle \frac{\partial \mathbf{u}}{\partial z} \right\rangle (z - h) & -h > z > -h - l \\ \mathbf{u}_{surf}^* + \left\langle \frac{\partial \mathbf{u}}{\partial z} \right\rangle l & -h - l \geq z \geq -H. \end{cases} \quad (1)$$

152 The piecewise function (1) includes two layers of depth-constant velocity and a sheared
 153 transition layer between them. Flow in the uppermost layer, which spans the depth of
 154 the ML $-h < z \leq 0$, is given by \mathbf{u}_{surf}^* . Here, h is defined as the depth at which T^*
 155 is 0.2°C colder than it is at 20 m depth. Below $z = -h$, we assume a transition layer
 156 of thickness $l = 30$ m (Johnston & Rudnick, 2009) and constant shear

$$\left\langle \frac{\partial \mathbf{u}}{\partial z} \right\rangle = 2H \frac{\mathbf{u}_{surf}^* - \mathbf{u}_{mean}^*}{[l^2 + 2l(H - l - h)]}. \quad (2)$$

157 The third layer extends down to $H = 180$ m and has velocities $\mathbf{u}_{surf}^* + \left\langle \frac{\partial \mathbf{u}}{\partial z} \right\rangle l$. This
 158 construction makes the depth-mean of \mathbf{u}^* between $z = 0$ and $z = -H$ strictly equal
 159 to \mathbf{u}_{mean}^* .

160 Concentrating vertical shear $\left\langle \frac{\partial \mathbf{u}}{\partial z} \right\rangle$ within a transition layer captures some of the
 161 main features of wind-forced currents. Thus, (1) and (2) yield an idealized 3D velocity
 162 field constrained by float velocity estimates and previous knowledge of the baroclinic re-
 163 sponse to TC forcing. However, it should be noted that high baroclinic modes that can-
 164 not be represented by (1). Likewise, small-scale vertical shear associated with turbulence
 165 is not resolved here. Instead, the characteristics of such fine scale processes will be de-
 166 scribed in section 4 using vertical profiles of T and S .

167 To finalize the reconstruction of 3D flows beneath Mangkhut from float measure-
 168 ments, we impose a condition of adiabatic continuity to obtain $\frac{\partial w^*}{\partial z} = -\frac{\partial u^*}{\partial x} - \frac{\partial v^*}{\partial y}$. Fur-
 169 thermore, we assume a rigid lid so that $w^*(z = 0)$ vanishes and $w^*(z < 0)$ at a given
 170 point (x, y) is

$$171 \quad w^*(z) = \int_0^z \left(\frac{\partial u^*}{\partial x} + \frac{\partial v^*}{\partial y} \right) dz'. \quad (3)$$

172 Before showing the interpolated fields T^*, S^*, u^*, v^*, w^* , we must emphasize that
 173 (1) the decorrelation scale $L = 150$ km suppresses high-frequency features in the ob-
 174 servations, and (2) some caution is warranted when interpreting results near the edge
 175 of the objective maps.

176 3 Mixed layer theory

177 In this section, we review the mechanisms of NIW generation by TCs and formu-
 178 late ML dynamics using vorticity ($\zeta = \nabla \times \bar{\mathbf{u}}$) and divergence ($\Gamma = \nabla \cdot \bar{\mathbf{u}}$) instead of
 179 depth-averaged ML currents $\bar{\mathbf{u}}$. As shown below, this simple change of variables leads
 180 to a set of ordinary differential equations describing inertial pumping, which must be oth-
 181 erwise described using partial differential equations (Gill, 1984). Lastly, numerical so-
 182 lutions of the (ζ, Γ, h) model are used to compare NIW generation under fast- and slow-
 183 moving TCs.

184 The dynamic response of $\bar{\mathbf{u}} = (\bar{u}, \bar{v})$ to a wind stress $\tau = (\tau_x, \tau_y)$ in a ML of thick-
 185 ness h can be described using the linear slab model in (4) and (5). Solutions to these equa-
 186 tions, first used by Pollard & Millard Jr (1970) to explain in-situ measurements, feature
 187 a slowly-varying component that approximates an Ekman balance and inertial oscilla-
 188 tions whose amplitude decays at a rate r . In order to resolve vertical velocities $\frac{\partial h}{\partial t}$ at the
 189 ML base, we couple (4) and (5) to the continuity equation (6). Here, $W_e \geq 0$ is an en-
 190 trainment rate used to represent ML deepening caused by turbulent mixing (Price, 1981).

$$191 \quad \frac{\partial \bar{u}}{\partial t} = f\bar{v} + \frac{\tau_x}{\rho_0 h} - r\bar{u} \quad (4)$$

$$192 \quad \frac{\partial \bar{v}}{\partial t} = -f\bar{u} + \frac{\tau_y}{\rho_0 h} - r\bar{v} \quad (5)$$

$$193 \quad \frac{\partial h}{\partial t} + h\nabla \cdot \bar{\mathbf{u}} = W_e \quad (6)$$

194 Because our focus here is on NIW generation, (4)-(6) exclude forces that make neg-
 195 ligible or secondary contributions to $\frac{\partial h}{\partial t}$. For example, barotropic flows develop in TC
 196 wakes (Shay & Chang, 1997), but the horizontal pressure gradients that drive them scale
 197 to make a negligible contribution to $\frac{\partial h}{\partial t}$ given the large horizontal scale of TCs (Geisler,
 198 1970; D'Asaro, 1989). Similarly, nonlinear solutions of $\frac{\partial h}{\partial t}$ under TCs (Price, 1981) show
 199 good agreement with the linear case solved by Geisler (1970), so advective terms $\bar{\mathbf{u}} \cdot \nabla \bar{\mathbf{u}}$
 200 and $\bar{\mathbf{u}} \cdot \nabla h$ can be dropped. Notice, however, that the local nonlinear effects of $h(t)$ on
 201 atmospheric forcing and continuity are preserved in (7) and (8). The limitations of our
 202 theoretical assumptions will be further discussed in Section 7.

203 When ML divergence $\Gamma = \nabla \cdot \bar{\mathbf{u}}$ oscillates at frequencies slightly greater than f ,
 204 periodic pumping of the ML base allows downward momentum transfer by NIWs (Price,
 205 1983; Gill, 1984). In the past, the baroclinic ocean response to TCs has been studied by
 206 coupling contiguous layers of increasing density through pressure gradients produced by
 207 interfacial displacements (Geisler, 1970; Price, 1981, 1983). Instead, (4) and (5) use the

208 empirical damping rate r to parameterize the downward propagation of internal waves,
 209 dissipation, and nonlinearities that drive Eulerian momentum decay in the ML (Pollard
 210 & Millard Jr, 1970; D’Asaro, 1985).

211 Historically, the value of r has been thought to be determined primarily by down-
 212 ward energy fluxes out of the ML (Gill, 1984; D’Asaro, 1985; Alford et al., 2016). In the
 213 mid latitudes, reduction of horizontal scales that enhances these fluxes largely depends
 214 on gradients in the mesoscale and planetary vorticity (Kunze, 1985; D’Asaro, 1989; John-
 215 ston et al., 2016; Asselin & Young, 2020). In contrast, the spatial structure of TC winds
 216 imprints sharp gradients on upper ocean currents and thus allows for immediate gener-
 217 ation of NIWs (D’Asaro, 1989). To emphasize this point, we now consider the ML re-
 218 sponse to TC forcing not in terms of \bar{u} and \bar{v} , but their spatial gradients.

219 3.1 Dynamics of wind-forced gradients in the upper ocean

220 Below, we manipulate (4)-(6) to isolate the components that contribute to $\frac{\partial h}{\partial t}$ and
 221 thus generate NIWs. To do this, we calculate $\frac{\partial \zeta}{\partial t} = \nabla \times \frac{\partial \bar{\mathbf{u}}}{\partial t}$ and study its relation to
 222 $\frac{\partial \Gamma}{\partial t} = \nabla \cdot \frac{\partial \bar{\mathbf{u}}}{\partial t}$. Taking the curl and divergence of (4) and (5) thus yields an alternative
 223 representation of ML dynamics

$$224 \quad \frac{\partial \zeta}{\partial t} = -f\Gamma + \frac{1}{\rho_0 h} \left(\nabla \times \tau - \frac{\tau}{h} \times \nabla h \right) - r\zeta \quad (7)$$

$$225 \quad \frac{\partial \Gamma}{\partial t} = f\zeta + \frac{1}{\rho_0 h} \left(\nabla \cdot \tau - \frac{\tau}{h} \cdot \nabla h \right) - r\Gamma \quad (8)$$

$$226 \quad \frac{\partial h}{\partial t} + h\Gamma = W_e. \quad (9)$$

227 This formalism does not explicitly include information about the magnitude and
 228 direction of currents. Instead, it uses the physical principles in (4)-(6) to resolve spatiotem-
 229 poral patterns in $\frac{\partial h}{\partial t}$, which ultimately contribute to internal wave generation. It is worth
 230 noting that, under axial-symmetric storms, $\nabla \cdot \tau$ and $\nabla \times \tau$ are fully determined by ra-
 231 dial and tangential winds respectively. Thus, (7) and (8) show how these separate com-
 232 ponents of τ directly drive orthogonal modes of motion ζ , Γ in the ocean.

233 In TC wakes, once winds cease to play a dominant role and the ML evolves freely,
 234 our diagnostic model (7)-(9) yields the three term balance in (10) and (11). This linear
 235 system of equations, a damped harmonic oscillator, produces inertial cycles in ζ and Γ
 236 with an exponential decay rate r . Inertial pumping arises directly from these cycles, which
 237 are simply a consequence of clockwise rotation in $\bar{\mathbf{u}}$.

$$238 \quad \frac{\partial \zeta}{\partial t} = -f\Gamma - r\zeta \quad (10)$$

$$239 \quad \frac{\partial \Gamma}{\partial t} = f\zeta - r\Gamma. \quad (11)$$

240 To visualize how (10) and (11) is an explicit statement of inertial pumping, we fol-
 241 low Gill (1984) and set $\tau = W_e = r = 0$ to consider the evolution of an initial condi-
 242 tion $\mathbf{u}(t_i)$ with $(\zeta_i, \Gamma_i) = (c_i, 0)$ where $c_i > 0$. As illustrated in Fig. 4, (10) and (11)
 243 imply that inertial rotation of current vectors transfers momentum from ζ into Γ , and
 244 from Γ into $-\zeta$ at time intervals $\frac{\pi}{2f}$. Quadrature between ζ and Γ in this oscillatory mode

245 means that NIW crests (troughs) must be surrounded by anticyclonic (cyclonic) iner-
 246 tial currents (Fig. 4). This correspondence between ζ and ML displacements has the im-
 247 portant implication that wind-driven, inertially-oscillating ML vortices and correspond-
 248 ing vertical displacements in the ocean interior can be sometimes mistaken for quasigeostrophic
 249 eddies.

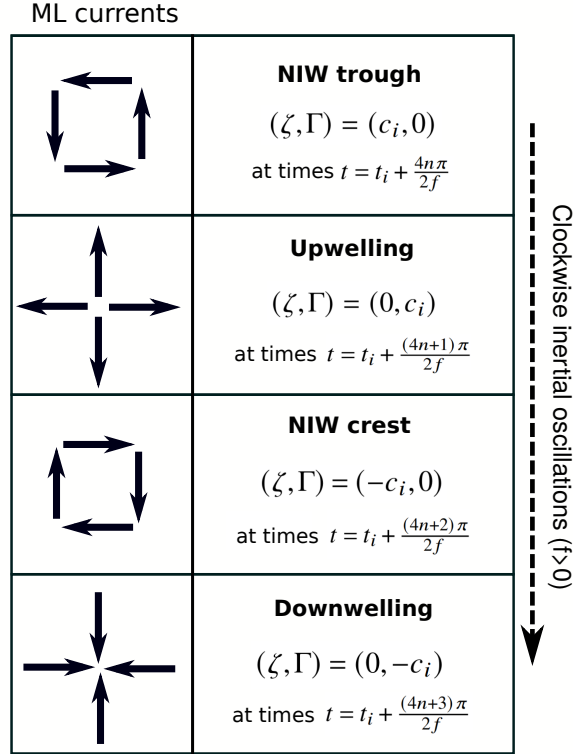


Figure 4. Successive rows illustrate the time evolution of current vectors under clockwise inertial oscillations. Starting from an initial condition $\mathbf{u}(t_i)$, corresponding values of (ζ, Γ) describe inertial pumping of h from (10) and (11). \mathbf{u} is depicted at $\frac{\pi}{2f}$ intervals ($n = 0, 1, 2, \dots$). Each 90° rotation fully transforms ζ into Γ , and Γ into $-\zeta$.

250 3.2 Relating upwelling and NIW generation to TC winds

251 When winds act on the ocean surface, $\bar{\mathbf{u}}$ initially accelerates in the direction of τ
 252 but is later steered in clockwise rotation by $f > 0$ (Ekman, 1905). Eventually, if winds
 253 persist unchanged over more than half an inertial period, the mixed layer will approach
 254 an Ekman balance where $(\bar{u}, \bar{v}) \sim \frac{1}{f\rho_0 h}(\tau_y, -\tau_x)$ is orthogonal to τ .

255 Setting $\nabla h = 0$ in (7)-(9), we may write Ekman's balance as $(\zeta, \Gamma) \sim \frac{1}{f\rho_0 h}(-\nabla \cdot$
 256 $\tau, \nabla \times \tau)$, so that Γ becomes sustained by $\nabla \times \tau$. However, notice that $\nabla \times \tau$ does not
 257 directly drive the evolution of Γ in (8). Instead, $\frac{\partial \zeta}{\partial t}$ and $\frac{\partial \Gamma}{\partial t}$ under τ will initially mir-
 258 ror patterns in $\nabla \times \tau$ and $\nabla \cdot \tau$ respectively. It is only later that the clockwise steering
 259 of currents by $f > 0$ gradually links $\nabla \times \tau$ to Γ and produces upwelling (Fig. 4).

260 The slow rate at which f steers $\bar{\mathbf{u}}$ away from the direction of τ gives rise to qual-
 261 itative differences between the ocean response to fast-moving and slow-moving storms.
 262 Using a two-layer model, Geisler (1970) showed that energy transfer into NIWs decreases
 263 with the ratio $U_{storm}/\|\mathbf{c}_g\|$, where $\|\mathbf{c}_g\|$ is the group speed of mode-1 internal waves. At

264 the limit where $U_{storm}/\|\mathbf{c}_g\| < 1$, Geisler’s solutions predict that the momentum in $\nabla \times$
 265 τ is entirely used by Ekman-style upwelling with no oscillatory behavior whatsoever. Nilsson
 266 (1995) later used a normal mode expansion approach to find supporting results in
 267 a continuously stratified fluid.

268 The formalism in (7)-(9) does not explicitly represent \mathbf{c}_g , but instead uses r to param-
 269 eterize its effects. Hence, we investigate whether this simple model of NIW generation
 270 can represent the transition between balanced and oscillatory regimes described
 271 by Geisler (1970) and Nilsson (1995). To do this, we used Euler’s method to compute
 272 point solutions (setting $\nabla h = 0$) of (7)-(9) under the forcing of Gaussian vortices $\nabla \times$
 273 τ with standard deviations of 2 and 6 hours to represent fast- and slow-moving TCs. These
 274 vortices represent the changing direction of tangential τ inside an axisymmetric TC eye
 275 but don’t include radial stresses, which are known to make only minor contributions to
 276 NIW generation (Price, 1983; Shay et al., 1989). The evolution of $(\zeta/f, \Gamma/f, h)$ from an
 277 initial condition $(0, 0, 80 \text{ m})$ under both scenarios is shown in Fig. 5.

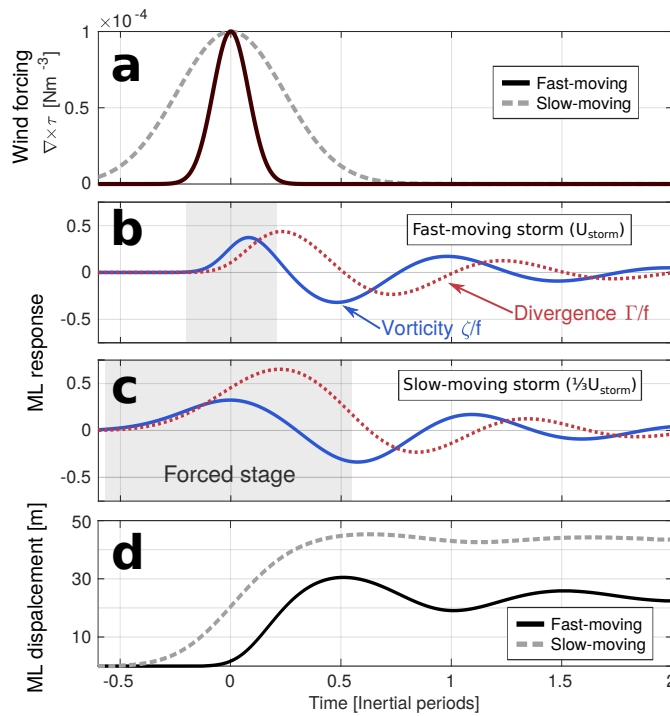


Figure 5. ML response (7)-(9) to (a) wind vortices representing (b) a fast-moving TC and (c) one moving at one-third the speed. (d) compares the mixed layer displacements $h(t_0) - h(t)$ that result from both simulations when $W_e = 0$. Gray shading in (b) and (c) marks the forced stage, which is followed by near-inertial pumping as given by (10) and (11).

278 Numerical solutions of (7)-(9) in Fig. 5 exemplify the two fundamental differences
 279 noted by Geisler (1970). Firstly, notice that the greatest upwelling (maximum Γ/f) oc-
 280 curs at the end of the forced stage for the fast-moving case (Fig. 5b), whereas Γ/f peaks
 281 well within the slow TC’s forced stage (Fig. 5c). Moreover, the net mixed layer displace-
 282 ment induced by the slow-moving TC is significantly greater than for the fast-moving
 283 case (Fig. 5d). This is consistent with a greater transmission of energy into balanced mo-
 284 tions (rather than inertial oscillations) for slowly-varying τ (Veronis, 1956; Pollard, 1970).

285 The second point of agreement between our simple model and Geisler’s solutions
 286 relates to the amplitude of NIWs generated by fast- and slow-moving TCs. Namely, the
 287 slow storm considered in Fig. 5 produced NIWs with a crest-to-trough amplitude of roughly
 288 5 m, less than half the amplitude of waves generated in the fast-moving case (Fig. 5d
 289 and Figs. 3-5 in Geisler 1970).

290 The model in (7)-(9) does not include the dynamical drivers of geostrophic adjust-
 291 ment and NIW propagation, which are important to arguments made by both Geisler
 292 (1970) and Nilsson (1995). Instead, their local effects are parameterized by r , which re-
 293 gulates the fraction of momentum that enters the damped oscillator in (10) and (11) at
 294 the end of the forced stage. As r decreases the amplitude of successive oscillations in (ζ, Γ) ,
 295 the downwelling portion of these cycles is necessarily smaller than the preceding upwelling.
 296 This process gradually leads to net upwelling (Fig. 5d), as momentum extracted out of
 297 ML inertial oscillations is used by thermocline NIWs and balanced motions (Rossby, 1938;
 298 Bolin, 1953; Gill, 1984).

299 The linear (ζ, Γ) view of ML dynamics (7)-(9) does not include any new physics
 300 absent from standard ocean models based on (u, v) . Rather, it uses a simple change of
 301 variables to elucidate linear 1D dynamical aspects that are not immediately evident in
 302 1D (u, v) -based models. Most importantly, it allows to explain inertial pumping (Fig.
 303 4) as a system of ordinary differential equations (10) and (11) rather than partial dif-
 304 ferential equations as done by Gill (1984). Moreover, example solutions in Fig. 5 sug-
 305 gest that the qualitative differences between the ocean response to fast- and slow-moving
 306 storms can be recovered from simpler principles than those used by Geisler (1970) and
 307 Nilsson (1995). This is in line with early analyses by Veronis (1956) and Pollard (1970),
 308 who argued that the partition of energy between geostrophically-adjusted motions and
 309 inertial oscillations is mainly set by the duration of τ rather than the underlying strat-
 310 ification.

311 4 Upper ocean dynamics beneath Mangkhut

312 We now turn our attention towards model output and observations of upper ocean
 313 dynamics beneath Super Typhoon Mangkhut. First, we present evidence supporting the
 314 validity of sampling and interpolation schemes described in Section 2. Second, the evo-
 315 lution of ζ and Γ in our observations is compared to the linear model (7)-(8) while T and
 316 S data confirm the generation of a large amplitude NIW as predicted by (9). Estimates
 317 of Γ and the corresponding w^* (3) are shown to be in agreement with observed isother-
 318 mal displacements and NIW generation behind Mangkhut. The role of turbulent mix-
 319 ing in changing h is discussed briefly but further details are given in the next section.

320 Hovmoller diagrams of $\bar{\mathbf{u}}$ and $(\zeta, \Gamma)/f$ in Figs. 6a,b show the ocean response to Mangkhut
 321 along 133°E in the coupled 3D model. Observational estimates \mathbf{u}_{surf}^* and \mathbf{u}_{mean}^* are shown
 322 with their corresponding $(\zeta, \Gamma)/f$ fields in Fig. 7. To compare model output and obser-
 323 vations, Fig. 6c shows a time series of the modelled $(\zeta, \Gamma)/f$ averaged between 14 and
 324 14.5°N (solid lines) and estimates ζ_{surf}^*/f along $y = 0$ (dashed lines). To help with com-
 325 parisons, the dashed rectangle in Fig. 6a represents the area shown in Fig. 7 and other
 326 visualizations of interpolated float measurements.

327 Quantitative agreement between ML current speeds in the model (Fig. 6a) and ob-
 328 servations (Fig. 7a) is good, with $\|\bar{\mathbf{u}}\|$ reaching $\sim 1 \text{ m s}^{-1}$ on the leading edge of the
 329 TC eye and $\sim 2 \text{ m s}^{-1}$ on the right side of the TC track. Qualitatively speaking, spa-
 330 tiotemporal patterns in \mathbf{u}_{surf}^* and \mathbf{u}_{mean}^* (Fig. 7a,b) are nearly identical to each other,
 331 suggesting that the effects of windage and wave motion on \mathbf{u}_{surf} do not drastically im-
 332 pact smoothed patterns in \mathbf{u}_{surf}^* . The greatest qualitative difference between modelled
 333 and observational velocity estimates is that inertial velocities $u \sim 1 \text{ m s}^{-1}$ appear in
 334 September 13 in Fig. 6a but are missing around the corresponding location $x = U_{storm} \frac{\pi}{f} =$

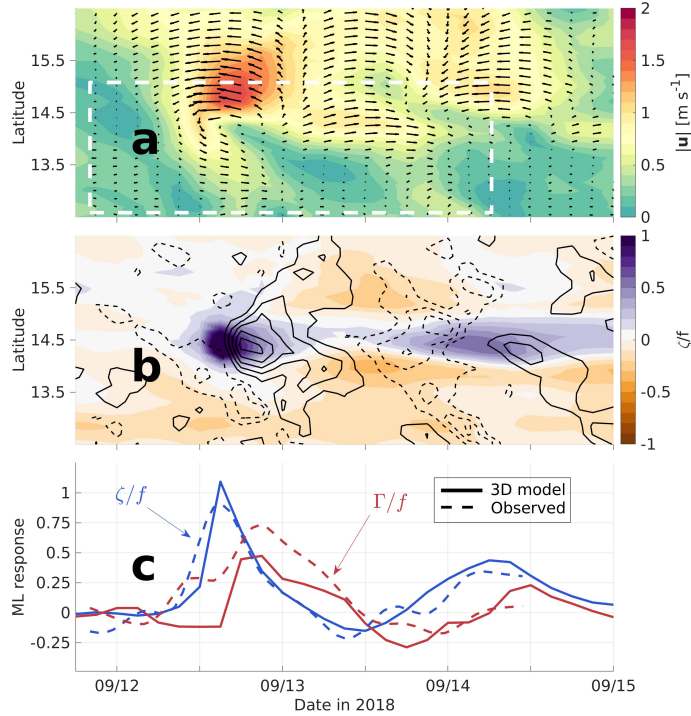


Figure 6. Time-latitude sections of the ML flow along 133°E in coupled 3D simulations of Mangkhut. Arrows and color shading in (a) show the direction and magnitude of $\bar{\mathbf{u}}$. Color shading in (b) shows ζ/f , while black contours denote $\Gamma/f \neq 0$ at 0.1 intervals (negative dashed). (c) compares model output of $(\zeta, \Gamma)/f$ averaged between 14 and 14.5°N (solid lines) to observational estimates made using \mathbf{u}_{surf}^* along $y = 0$ (dashed lines). The dashed rectangle in (a) is representative of the area shown by Fig. 2b and visualizations of interpolated data.

335 500 km in Fig. 7a. Despite this one difference, general agreement between observations
 336 and model output suggests that the sampling and interpolation scheme described in Sec-
 337 tion 2 appropriately captures the primary characteristics of upper ocean response to TC
 338 forcing. Yet, it is uncertain how windage and wave motion impact the accuracy of mea-
 339 surements \mathbf{u}_{surf} under different flow regimes.

340 In both the observational records and the model, ζ/f peaked during TC passage
 341 and later evolved in quadrature with Γ/f as the amplitude of oscillations decayed (Figs.
 342 6b,c, 7c,d). Ocean currents near the TC eye were dominated by a vortical core with $\zeta_{model}/f \sim$
 343 1 , $\zeta_{surf}^*/f \sim 1$ and $\zeta_{mean}^*/f \sim 0.4$ (color shading in Figs. 6b, 7c,d). Wind-forced vor-
 344 tices later evolved into divergent maxima $\Gamma_{model}/f \sim 0.5$, $\Gamma_{surf}^*/f \sim 0.7$ and $\Gamma_{mean}^*/f \sim$
 345 0.4 near $x = 150$ km (black contours in Figs. 6b, 7c,d). Local minima in ζ/f trail the
 346 TC around $x = 450$ km. As described in Section 3, vortical currents near the TC eye cor-
 347 respond to the ocean’s immediate response to $\nabla \times \tau$ (7), while subsequent coupled os-
 348 cillations in ζ/f and Γ/f result from the clockwise rotation of current vectors (Figs. 4,
 349 5).

350 Overall, there is good agreement between (ζ, Γ) in the 3D model and observations
 351 (Fig. 6c). However, estimates of Γ/f differ significantly near the leading edge of the TC
 352 eye, where $\Gamma_{surf}^*/f \sim 0.25$ but $\Gamma_{model}/f \sim -0.1$. It is unclear whether this difference
 353 results from imperfect sampling and interpolation of float data, preexisting ocean con-
 354 ditions missing from the 3D model, or inaccuracies in the modelled surface winds.

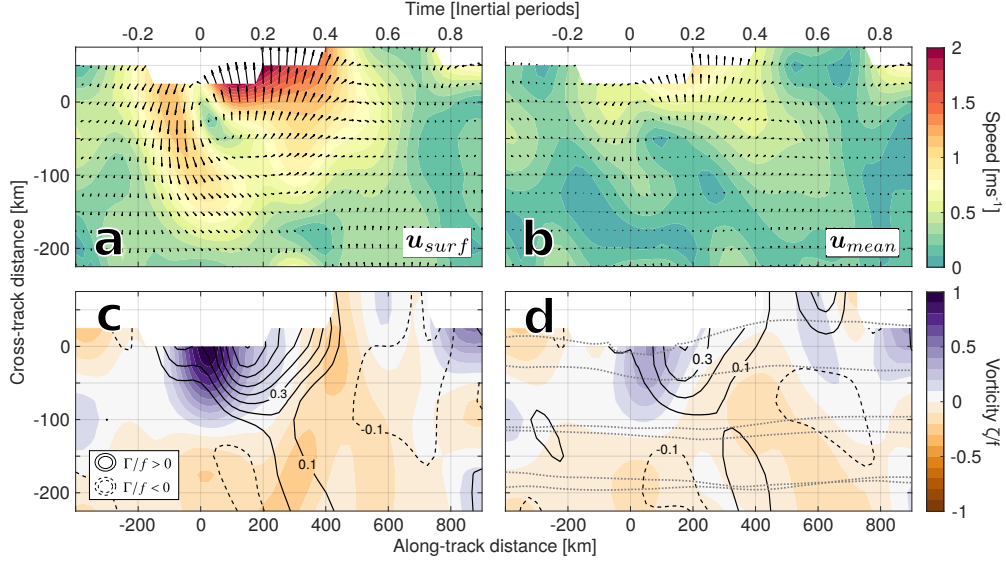


Figure 7. Two-dimensional maps of \mathbf{u}_{surf} (left) and \mathbf{u}_{mean} (right) are viewed through their speed and direction (**a**, **b**) and their ζ, Γ components (**c**, **d**). Color in **c** and **d** shows ζ_{surf}/f and ζ_{mean} respectively, while Γ_{surf}/f and Γ_{mean}/f are shown in black contours. Contours are continuous for upwelling-favorable values $\Gamma/f > 0$, while dashed contours show $\Gamma/f < 0$. Dotted lines (**d**) show the float tracks.

355 With the validity of our observational technique supported by model output and
 356 by similarities between \mathbf{u}_{surf}^* and \mathbf{u}_{mean}^* , we now test whether the simple model in (7)
 357 and (8) can reproduce observed cycles in $(\zeta_{surf}^*, \Gamma_{surf}^*)/f$. Moreover, we use $T^*(x, y, z)$
 358 to test the relation (9) between ML dynamics and NIW generation. To do so, we take
 359 interpolated float data along $y = 0$ and compare observations to numerical solutions
 360 of (7)-(9) under idealized TC forcing with a damping rate $r = 0.5f$ (Fig. 8).

361 Atmospheric forcing $\nabla \times \tau$ in Fig. 8 corresponds to the reversal of tangential wind
 362 between opposite sides of the TC eyewall. The magnitude of $\nabla \times \tau$ used here agrees with
 363 the mean wind stress curl $\frac{|\tau_{max}|}{MWR} = 2.24 \times 10^{-4} \text{ N m}^{-3}$ inside the TC eye (dashed line).
 364 Here, $MWR = 40 \text{ km}$ is the maximum wind radius, while $|\tau_{max}| = C_D \rho_{air} |U_{10}|^2$ was
 365 calculated using $U_{10} = 70 \text{ m s}^{-1}$ (Fig. 1), $\rho_{air} = 1.22 \text{ kg m}^{-3}$, and $C_D = 1.5 \times 10^{-3}$
 366 kg m^{-3} (Zweers et al., 2010).

367 The magnitude of convergent stresses $\nabla \cdot \tau < 0$ is set to be artificially low in these
 368 simulations (Fig. 8a). Although $\|\nabla \cdot \tau\| \sim \|\nabla \times \tau\|$ in the 3D atmospheric model, a
 369 great deal of the momentum that $\|\nabla \cdot \tau\|$ imparts on Γ is rapidly countered by nonlin-
 370 ear effects and thus does not contribute significantly to NIW generation in the TC wake
 371 (Price, 1983). Lastly, it should be noted that forcing in Fig. 8a ignores the gradual weak-
 372 ening of τ far from the eyewall, where $\nabla \times \tau < 0$ and $\nabla \cdot \tau > 0$.

373 Agreement between linear solutions and observations in Fig. 8 confirms that clock-
 374 wise rotation of $\bar{\mathbf{u}}$ (Fig. 2b) transformed the wind-forced ζ/f into Γ/f near the end of
 375 the forced stage. Momentum in Γ/f was later transferred to an inertial anticyclone $\zeta/f <$
 376 0 and the cycle continued as shown schematically in Fig. 4.

377 Observations show that the 27°C isotherm deepened by $\sim 25 \text{ m}$ under the TC eye
 378 before it traveled up 75 m as predicted by linear theory (Fig. 8c). Initial deepening may
 379 be partially explained by turbulent mixing, which is evidenced by Thorpe scale estimates

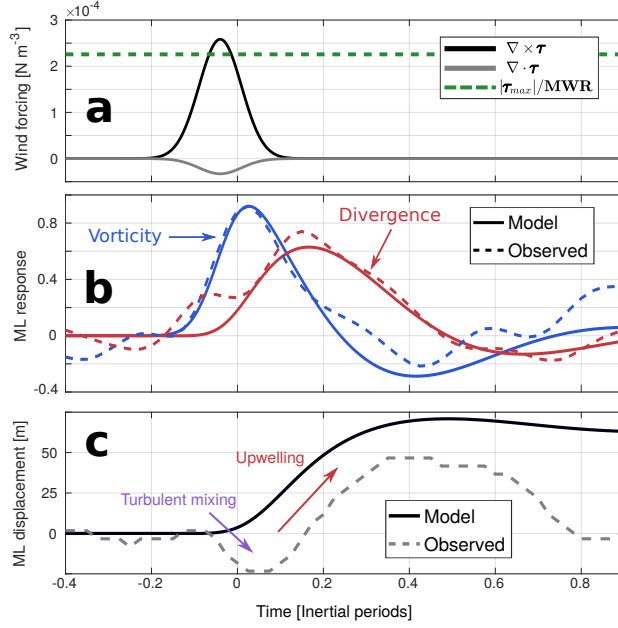


Figure 8. ML response to idealized TC-like atmospheric forcing. Numerical solutions of (7)-(9) setting $W_e = \nabla h = 0$ were obtained using the wind forcing terms in panel **a**. **(b)** compares solutions to estimates of ζ/f (blue) and Γ/f (red) made using \mathbf{u}_{surf}^* (Fig. 7c) along $y = 0$ km. Linear solutions of $h(t)$ (**c**, solid line) agree with observed displacements of the 27°C isotherm (dashed line).

380 of diffusivity $10^{-5} < \kappa < 1 \sim$ around $x = 0$ km (Fig. 9b). These estimates relate the
 381 potential energy stored within unstably stratified regions to a dissipation rate ε that is
 382 then substituted to calculate $\kappa = \frac{1}{5} \frac{\varepsilon}{N^2}$ as described by S. A. Thorpe (1977); A. F. Thomp-
 383 son et al. (2007) where N is the buoyancy frequency.

384 Agreement between the slopes $\frac{\partial h}{\partial t}$ in the upwelling portion of Fig. 8c suggests that
 385 measurements Γ_{surf}^* are accurate there. Moreover, it implies that upwelling in the wake
 386 of Mangkhut resulted from the near-inertial coupling of ζ/f and Γ/f , marking the gener-
 387 ation of a large amplitude NIW. The modelled Γ/f agrees well with Γ_{surf}^* for all $t >$
 388 0 (Fig. 8b). Nonetheless, both estimates failed to capture the magnitude of $\Gamma/f < 0$
 389 implied by the downward displacement of h observed starting at $t \approx 0.6$ inertial peri-
 390 ods (Fig. 8c). Namely, convergence ($\Gamma_{surf}/f \sim -0.15$) in the first downwelling por-
 391 tion of the NIW wake is underestimated by observations, where $\Gamma_{model}/f \sim -0.25$ (Fig.
 392 6c).

393 Inferred profiles of w^* and u^* in Fig. 9a reveal the structure of upwelling in the wake
 394 of Mangkhut. With w^* reaching 8 m h^{-1} , isotherms were lifted by as much as 75 m around
 395 $x = 350$ km. T^* shows that isotherms had been lifted by ~ 20 m near the end of the
 396 first NIW cycle ($x = 850$ km, Fig. 9a). This net upwelling is crucial to the process of
 397 geostrophic adjustment (Geisler, 1970; Nilsson, 1995), and determined in (8)-(9) by the
 398 magnitude of r .

399 To test the impacts of advection in setting the ocean stratification behind Mangkhut,
 400 as well as the accuracy of inferred 3D flows (Eqs. 1-3), Fig. 9c shows the Eulerian heat-
 401 ing rate $\frac{\partial H_e}{\partial t} = \rho_0 C_p \frac{\partial T^*}{\partial t}$ calculated along $y = 0$ through two different methods. First,
 402 we used a frozen field assumption so that $\frac{\partial T^*}{\partial t} = U_{storm} \frac{\partial T^*}{\partial x}$ (color shading). Second,

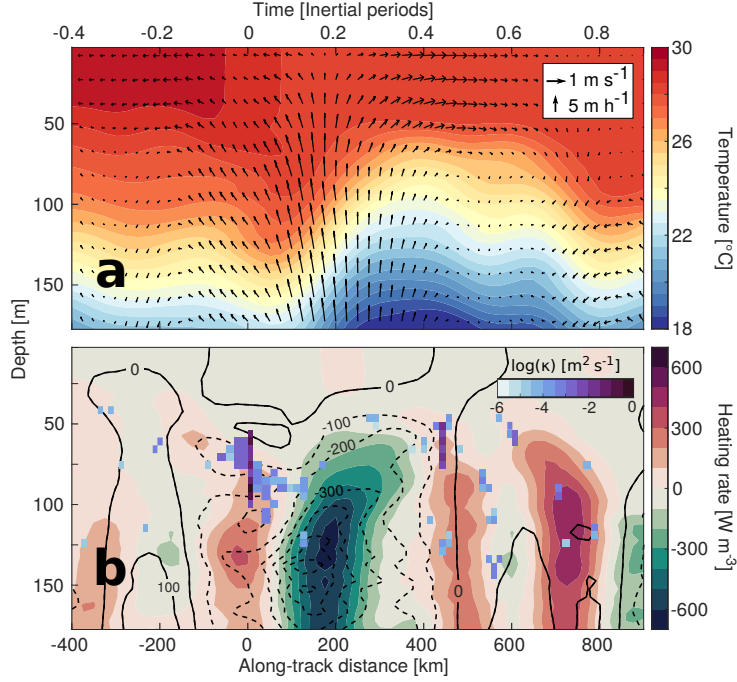


Figure 9. Vertical sections of T^* and (u^*, w^*) along $y = 0$ (a) show the generation of a NIW behind Super Typhoon Mangkhut. The vertical component w^* is magnified for clarity. (c) shows frozen field estimates (color shading) and advective contributions (contours at 100 W m^{-3} , dashed for negative values) to the Eulerian heating rate $\frac{\partial H_c}{\partial t}$, while estimates of κ indicate the intensity of vertical mixing inferred from M3 (note the log scale).

403 we used \mathbf{u}^* and w^* to calculate the advective contribution $\frac{\partial T^*}{\partial t} \approx -u^* \frac{\partial T^*}{\partial x} - v^* \frac{\partial T^*}{\partial y} -$
 404 $w^* \frac{\partial T^*}{\partial z}$ (black contours). $\frac{\partial H_c}{\partial t}$ below the ML is dominated by the term $w^* \frac{\partial T^*}{\partial z}$, so the color
 405 shading and black contours in Fig. 9b agree in areas where the inferred w^* yields a good
 406 approximation. Agreement is particularly good near $x = 180 \text{ km}$, where upwelling caused
 407 $\frac{\partial H_c}{\partial t} \sim -500 \text{ W m}^{-3}$. As described above, float data underestimate convergence and the
 408 corresponding $\frac{\partial H_c}{\partial t} > 400 \text{ W m}^{-3}$ in the downwelling region around $x = 700 \text{ km}$.

409 Advective estimates of $\frac{\partial H_c}{\partial t}$ mistakenly predict cooling below 75 m depth around
 410 $x = 0$, where T^* shows heating rates as high as 300 W m^{-3} (color shading). Disagree-
 411 ment between observed heating and advective estimates below the TC eye may be ex-
 412 plained by a possible bias in Γ_{surf}^* (Fig. 6c) but also by vigorous mixing. Thorpe esti-
 413 mates of κ in Fig. 9b reveal areas where enhanced values of κ could invalidate the as-
 414 sumption that $\frac{\partial H_c}{\partial t}$ was dominated by advection.

415 While variations in the ML flow are dominated by near-inertial oscillations (Fig.
 416 8), $\frac{\partial H_c}{\partial t}$ shows the signature of super-inertial motions (Fig. 9b). Horizontal sections of
 417 $\zeta/f, \Gamma/f$, and $N^* = \sqrt{-\frac{g}{\rho_0} \frac{\partial \rho^*}{\partial z}}$ taken at 160 m depth (Fig. 10) feature nearly paral-
 418 lel, periodic stripes that move away from the storm track towards $y < 0$. While ζ/f
 419 and Γ/f are linked by the rotation of current vectors (Fig. 4), Γ and N are linked by
 420 isopycnal displacement and stretching. Therefore, these three variables offer complemen-
 421 tary views of internal wave phase propagation.

422 Color shading in Fig. 10c shows the magnitude $\|\mathbf{u}_{surf}^* - \mathbf{u}_{mean}^*\|$ as a proxy for
 423 vertical shear below the ML. As evidence of areas of shear instability, Thorpe scale es-

424 timates ε show clusters of unstable overturns ahead of, directly beneath, and behind Mangkhut.
 425 These indicate that mixing was greatest within 100 km of the TC eye (Fig. 9b). How-
 426 ever, notice that unstable overturns in $x > 0$ km are preferentially distributed along
 427 the tilted phase lines in ζ/f , Γ/f , and N (Fig. 10c).

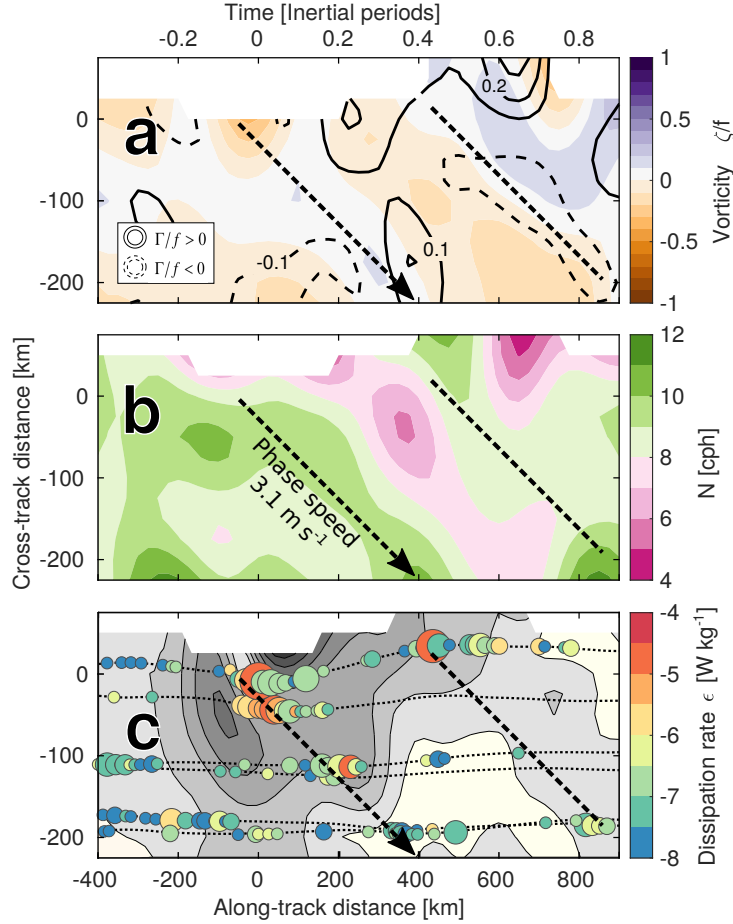


Figure 10. Horizontal sections of ζ , Γ (a), and N (b) at 160 m. The color of circles in panel c show depth-averaged estimates of ε , while their size indicates the height of overturns (range is between 5 and 25 m). Gray shading in (c) shows $\|\mathbf{u}_{surf}^* - \mathbf{u}_{mean}^*\|$ as a proxy for vertical shear at the mixed layer base. Thin, dotted lines denote individual float tracks.

428 Starting near the TC eye, all 6 floats sampled the first of these narrow fronts of static
 429 overturns. After half an inertial period, 3 floats measured a similar streak of enhanced
 430 turbulence extending from $(x = 450 \text{ km}, y = 25 \text{ km})$ to $(x = 900 \text{ km}, y = -200 \text{ km})$.
 431 A third parallel streak of density overturns was observed from $(x = 1000 \text{ km}, y = 50 \text{ km})$
 432 to $(x = 1250 \text{ km}, y = -100 \text{ km})$ but is beyond the domain shown here. The tilt
 433 of these lines corresponds to a propagation velocity $\sim 3.1 \text{ m s}^{-1}$ in the cross-track di-
 434 rection (dashed lines in Fig. 10), which is within 5% of the climatological $\|\mathbf{c}_g\|$ in the
 435 Philippine Sea (Chelton et al., 1998).

436 Given the similarities between spatial patterns in turbulent overturns and lines of
 437 equal phase in Γ , ζ , N , Fig. 10c suggests that enhanced ocean mixing in the TC wake
 438 was modulated by the phase of mode-1 NIWs and internal waves of frequency $\sim 2f$. Super-
 439 inertial waves are generated in TC wakes by the advection of spatial gradients in the ML

440 flow (Niwa & Hibiya, 1997; Zedler, 2009). Observations in Fig. 10 thus point to the po-
 441 tential influence of nonlinear dynamics and preceding oceanic conditions not represented
 442 in (7)-(9). As these waves propagated into the thermocline and away from the TC track,
 443 their mixing would have presumably caused remote impacts to ocean stratification.

444 5 Upper ocean thermodynamics beneath Mangkhut

445 5.1 Mixed layer deepening and turbulent entrainment

446 Space-time variations in T and S under the sea surface result from 3D advection,
 447 mixing, and interactions with the atmosphere. In the case of intense, fast-moving TCs
 448 like Mangkhut, shear-driven mixing at the ML base is expected to dominate upper ocean
 449 cooling (D’Asaro, 2003; Vincent et al., 2012). This process is evidenced by float mea-
 450 surements of T averaged between 0.5 and 1.5 m depth (Fig. 11a), which show a gener-
 451 alized cooling trend during storm passage. In particular, 1-m binned profiles of T , S and
 452 potential density (σ_0) from float M3 show a clear, gradual deepening of the ML base be-
 453 tween $x = -250$ km and the TC eye (Figs. 11b-d).

454 Successive float profiles in Figs. 11b-d show decreases in SST but increases in both
 455 sea surface salinity (SSS) and σ_0 as the ML deepened. This corresponds to entrainment
 456 of cold, salty water from below. As further evidence of the vigorous turbulence that trans-
 457 formed ocean thermodynamics beneath Mangkhut, vertical profiles of σ_0 feature ~ 10 -
 458 m tall regions with unstable stratification (i.e. $\frac{\partial \sigma_0}{\partial z} > 0$, Fig. 11d). Thorpe scale estimates
 459 of ε indicate the contribution of these density overturns to ocean turbulence (S. Thorpe,
 460 1973).

461 After storm passage, SSS (SST) had increased (decreased) for all floats (Figs. 11a,
 462 12a), indicating widespread mixing of the upper ocean beneath Mangkhut. The influ-
 463 ence of precipitation is also shown in Fig. 12a, as floats M5, M6 and M7 sampled sharp
 464 decreases in SSS between $x = -250$ and $x = -150$ km. To examine the impacts of
 465 rainfall in near-surface T and S , we interpolated data from the Integrated Multi-Satellite
 466 Retrievals for Global Precipitation Measurement (IMERG, Huffman et al. (2015)) onto
 467 the times and locations of float measurements. Estimated hourly rates of precipitation
 468 (size of circles) and cumulative rainfall integrated since $x = -400$ km (color) show that
 469 all floats experienced significant precipitation (Fig. 12b). However, and despite encoun-
 470 tering more rainfall than any other floats, M1 and M3 timeseries of SSS do not feature
 471 significant decreases attributable to precipitation (Fig. 12b).

472 In order for precipitation to impact SSS data, surface rain layers must form and
 473 remain stable for long enough (> 30 minutes) to be sampled by floats. However, this is
 474 only possible when buoyancy production by rainfall is greater than buoyancy mixing rates
 475 that diffuse salinity gradients (E. J. Thompson et al., 2019). Namely, there exist wind
 476 speed thresholds for which freshwater inputs are mixed into the ML more rapidly than
 477 observations can resolve. This leads to the interpretation that floats M1 and M3 did not
 478 measure significant SSS freshening (Fig. 12a) due to increased wind speeds and corre-
 479 sponding turbulence near the TC track (Price, 1981).

480 Successive profiles of T and S retrieved by float M7 (Fig. 13) detail the process of
 481 rain layer formation and their subsequent destruction via mixing. At the beginning of
 482 this sequence (Figs. 13a,b), consecutive float profiles ranging from $x = -246$ to $x =$
 483 0 km show a well-mixed upper ocean with no vertical gradients in T or S . Later on (Figs.
 484 13c,d), a layer of water with low T and S formed in the upper 5 m around $x = -140$
 485 km (black line) but was gradually mixed and deepened over the following casts. This rain
 486 layer accounts for the sharp decrease in SSS measured by M7 (Fig. 12a), while the sub-
 487 sequent increase in SSS was caused by mixing of cold, salty water from below. Roughly

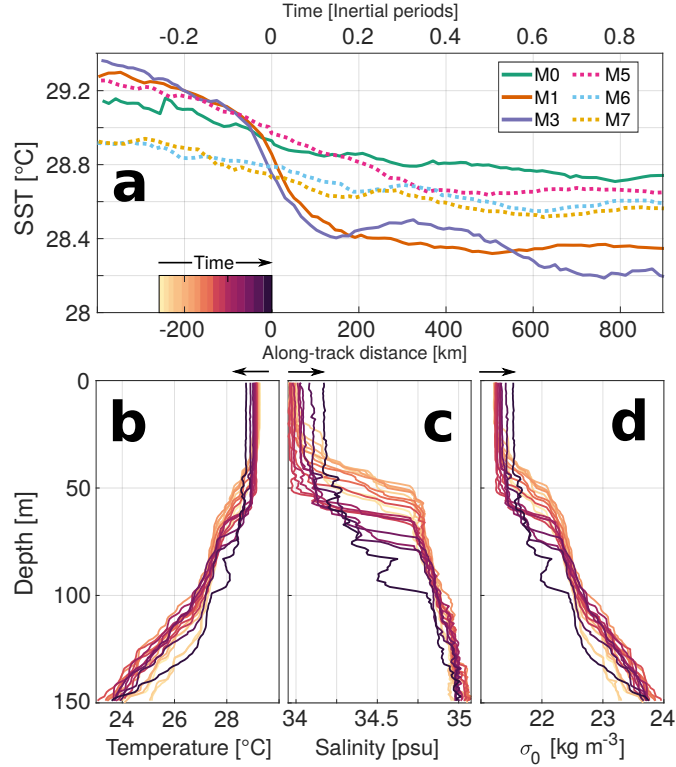


Figure 11. SST measured by all floats is shown as a function of along-track distance in panel **a**. 1-m binned profiles of temperature (**b**), salinity (**c**) and density (**d**) measured by float M3 show the mixed layer deepening. Individual profiles shown in the lower panels are color coded by their corresponding along-track distance as shown in panel **a**.

488 four hours (near $x = -50$ km) after its formation, there was little to no indication left
 489 that a rain layer had formed around float M7 (Figs. 13e,f).

490 Consistent with Thorpe scale estimates (Fig. 9b), interpolated fields $T^*(x, y)$ and
 491 $S^*(x, y)$ in Fig. 14 suggest that maximum mixing rates occurred within 100 km of the
 492 TC eye. Anomalies in T^* and S^* are asymmetric around the TC track, in agreement with
 493 greater windwork (Chang & Anthes, 1978; Price, 1981) and current speeds for $y > 0$
 494 (Figs. 6a, 7a,b). Although floats preferentially sampled the left side of the storm and
 495 interpolated fields can become unreliable beyond the edges of our sampling area, mea-
 496 surements from floats M1 and M3 offer nearly symmetric coverage of near-surface con-
 497 ditions within 50 km of the storm track (Fig. 2b). SST cooling and SSS changes mea-
 498 sured by M3 were consistently greater than for M1 (Figs. 11a, 12a), supporting the right-
 499 ward bias in Fig. 14a. Overall, changes in ML T and S under Mangkhut are fully con-
 500 sistent with shear-driven entrainment of cold, salty waters across the ML base.

501 5.2 Turbulent ocean heat pump

502 While TC-driven turbulence is most recognized for cooling SST during the forced
 503 stage (Fig. 14a), TCs cause long-lasting impacts on upper ocean thermodynamics (John-
 504 ston et al., 2020). Many studies have explored the long-term consequences of TC-driven
 505 mixing and its potential contribution to shape tropical ocean circulation (K. Emanuel,
 506 2001; Srivier & Huber, 2007; Mei et al., 2013). However, quantifying the buoyancy and
 507 heat gained by the tropical thermocline due to TC mixing requires making assumptions

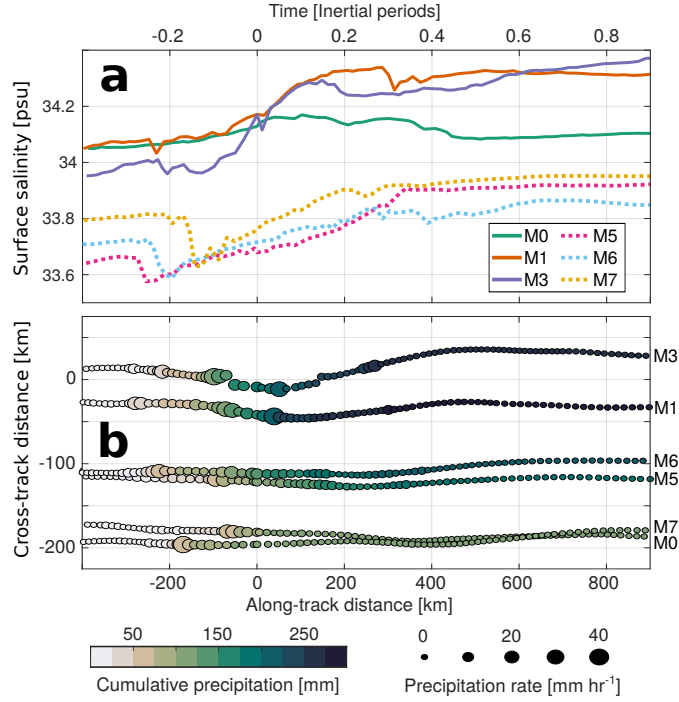


Figure 12. Mean S in the upper 5 m along the float tracks (a). IMERG data show precipitation rates and cumulative rainfall along float trajectories (b). As expected, greater values of time-averaged precipitation appear closer to the typhoon eye.

508 about the magnitude, extent, and persistence of enhanced κ . Empirical estimates of κ
 509 beneath TCs can thus provide insight into the duration and intensity of turbulent heat
 510 fluxes thought to shape global ocean heat transport.

511 Changes in T-S relationships can inform about the magnitude and vertical extent
 512 of anomalous κ and other diabatic processes (Hautala et al., 1996; Alford et al., 1999;
 513 Moum et al., 2003). T-S relations in our data (Fig. 15) result from a combination of tur-
 514 bulance, 3D advection, and atmospheric fluxes. Fortunately, turbulence and advection
 515 can be differentiated by their characteristic effects on T-S plots (Hautala et al., 1996).

516 The progression of water-mass properties measured by floats M1 and M3 through-
 517 out 200 km-long segments is color-coded in Fig. 15a. By comparing the time-averaged
 518 T-S properties sampled at different stages of storm passage, we may infer the processes
 519 that caused observed transformations. For example, average profiles measured by float
 520 M3 within the range $200 \leq x \leq 400$ km (dashed blue line) are compared to data from
 521 $400 \leq x \leq 600$ km (solid line) in Fig. 15b.

522 In order to determine the effects of mixing in the transition between these two pro-
 523 files in Fig. 15b, we used averaged T-S relations from 200-400 km as the initial condi-
 524 tion in a diffusive model with constant κ

$$\frac{\partial T}{\partial t} \sim \kappa \frac{\partial^2 T}{\partial z^2} \quad (12)$$

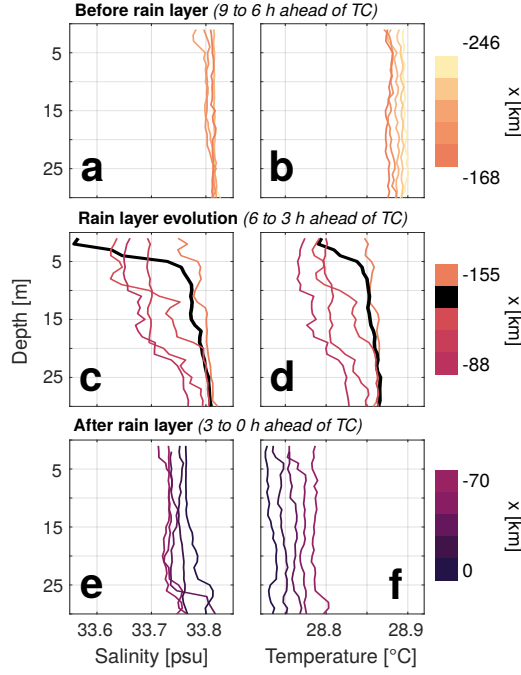


Figure 13. Evolution of a rain layer in three stages. Each row shows 5 consecutive profiles of T and S (color-coded by along-track position x) taken over a ~ 3 h period. Upper panels show vertical profiles of S (a) and T (b) measured by float M7 before SSS was significantly affected by rainfall. The middle panels show a rapid decrease in near-surface salinity (c) and temperature (d). Initially, freshwater anomalies were confined to the upper 5 m (black line), but were later diffused across a greater depth (maroon lines). On panels e and f, turbulent mixing has mostly de-stratified the upper ocean.

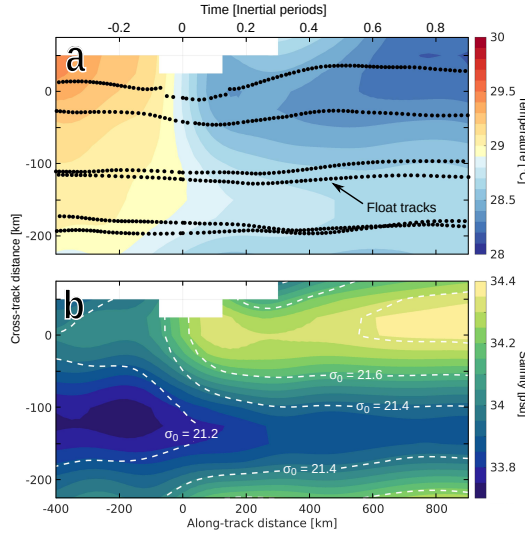


Figure 14. Plan view of T^* (a) and S^* (b) averaged over the upper 5 m. Black dots in panel a show the locations of each profile, while dashed contours in (b) show values of σ_0 [kg m^{-3}].

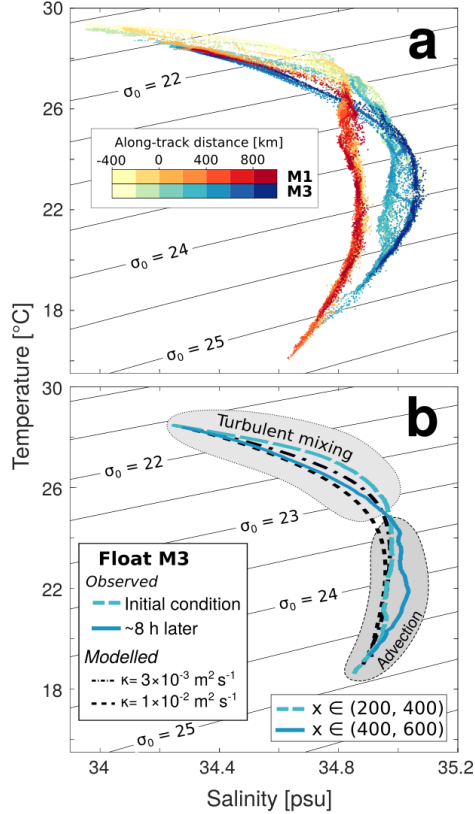


Figure 15. T-S profiles measured by floats M1 and M3 are color-coded by along-track distance in panel **a**. Mean profiles measured between 200 and 400 km (dashed line) and between 400 and 600 km (solid line) in **b** show transformations caused throughout an 8 h period. Black dashed lines show T-S properties modelled using (12) and (13) under the initial condition $x \in (200, 400)$ and different values of κ .

$$\frac{\partial S}{\partial t} \sim \kappa \frac{\partial^2 S}{\partial z^2}. \quad (13)$$

Time evolution in (12) and (13) ignores 3D advection and air-sea fluxes, and can thus only approximate T-S transformations at depths for which mixing dominated $\frac{\partial T}{\partial t}$ and $\frac{\partial S}{\partial t}$. T-S properties that result from applying $\kappa = 3 \times 10^{-3}$ and $1 \times 10^{-2} \text{ m}^2 \text{ s}^{-1}$ over 8 h (0.2 inertial periods) are shown with black dashed lines in Fig. 15b. These solutions of (12) and (13) agree well with the observed T-S changes for $\sigma_0 < 23.2 \text{ kg m}^{-3}$ but fail to explain observations of greater density classes (Fig. 15b). For $\sigma_0 > 23.5 \text{ kg m}^{-3}$, S increased beyond the range of S in the initial condition. Such a transformation requires input of high- S water from elsewhere and hence cannot result from vertical mixing. Together, these features suggest that between $x = 200$ and $x = 600$ km, mixing dominated watermass transformations down to ~ 110 m depth and 3D advection had greater impacts below that.

Values of $\kappa > 10^{-3} \text{ m}^2 \text{ s}^{-1}$ inferred from this analysis are greater than the majority of Thorpe scale estimates between $x = 200$ and 600 km, whose average value is $7.1 \times 10^{-4} \text{ m}^2 \text{ s}^{-1}$ (Fig. 9b). However, these estimates are not necessarily contradictory, as ocean turbulence is highly intermittent and follows a log-normal-like distribu-

tion (Pearson & Fox-Kemper, 2018; Cael & Mashayek, 2021). Thus, the effective κ over long periods of time (Fig. 15b) is disproportionately determined by relatively few mixing events with high κ and thousands of point measurements (Fig. 9b) are necessary to produce accurate statistics (Baker & Gibson, 1987). Therefore, estimates of κ across individual mixing events (Fig. 9b) are expected to have lower magnitudes than κ derived from analyses of watermass transformation (Fig. 15), which help infer effective or time-averaged values of κ .

6 Discussion

Linear dynamics presented in Section 3 neglect the effects of advection and pressure gradients. However, model output and float observations (Figs. 6, 8) indicate that (7)-(9) capture the primary mechanisms of NIW generation by TCs. As illustrated in Fig. 4, this means that clockwise inertial rotation of ML currents in the TC wake transforms ζ into Γ and Γ into $-\zeta$. Beginning with the conversion of wind-forced ζ into Γ during the second half of the forced stage, coupling between these modes leads to inertial pumping of the ML and the generation of a NIW (Figs. 8, 9).

Using idealized TC forcing with $|\nabla \times \tau| \gg |\nabla \cdot \tau|$, the linear model (7)-(9) reproduced NIW generation as seen in observations of ζ , Γ , and h (Fig. 8). This is in line with earlier model descriptions assessing that, although $\nabla \times \tau$ and $\nabla \cdot \tau$ have similar magnitudes under TCs, the latter has a minor role in NIW generation (Price, 1983; Shay et al., 1989). While the model (7)-(9) is only a reformulation of the slab model presented by Pollard & Millard Jr (1970), its simplicity can help conceptual understanding of the mechanisms that govern NIW generation and upwelling beneath TCs.

Reconstructed 3D fields of \mathbf{u}^* , T^* , and S^* are in good qualitative agreement with previous knowledge of the ocean response to TCs as well as with each other. For example, observational estimates of Γ/f appeared to be confirmed by model output (Fig. 6) and linear theory (Fig. 8b), but can also reproduce information in T^* between $t = 0.1$ and 0.5 inertial periods after TC passage (Fig. 8c). Likewise, the asymmetric distribution of windwork evidenced by \mathbf{u}_{surf}^* and \mathbf{u}_{mean}^* (Fig. 7a,b) is consistent with asymmetric changes in SST and SSS (Figs. 14).

General agreement with the 3D model (Figs. 6, 7) and physically-sensible relations between reconstructed variables supports our treatment (Section 2) of autonomous profiler data as a viable framework to study the ocean response to TCs. Past studies have inferred the 3D structure of upper ocean features powered by TCs (Jacob et al., 2000; ?); however, the (ζ, Γ) framework adopted here (Figs. 4, 8, 10) and mixing analyses (Figs. 9, 10, 15) yield additional dynamical insights.

Validity of float estimates ζ and Γ at later stages of NIW evolution is uncertain, as floats failed to capture convergence necessary to produce downwelling inferred from T^* (Figs. 8c, 9). This may be due to inaccuracies in measurements \mathbf{u}_{surf} or to the loss of coherence in NIWs in the TC wake. Spatially varying biases in $(\zeta_{surf}, \Gamma_{surf})/f$ affect the value $r = 0.5f$ used for numerical solutions in Fig. 8, which is considerably higher than values $\sim 0.2f$ commonly used to reproduce $\bar{\mathbf{u}}$ observed under extratropical storms (Pollard & Millard Jr, 1970; D'Asaro, 1985; Alford, 2001). Guan et al. (2014) estimated $r = 0.7f$ in the wake of a TC, and argued that increased Eulerian momentum decay was caused by interactions with the background internal tides. Conversely, Kundu & Thomson (1985) proposed that NIWs decay more rapidly behind TCs than they do behind extratropical cyclones given the point-source nature of TC forcing. However, sampling biases make it such that the value $r = 0.5f$ used here does not necessarily imply an anomalous rate of ML momentum decay behind Mangkhut.

Evidence of cycles in ζ and Γ was found in both the ML (Figs. 7, 8) and the thermocline (Fig. 10). The latter revealed the cross-track propagation of internal waves with frequency $\sim 2f$ and associated modulation of ε . Prior observations have shown that ocean turbulence is modulated by the phase of internal waves (Alford & Gregg, 2001; Mounm et al., 2003), but phase-locked mixing within TC wakes (Fig. 10.c) had not been reported previously. This result supports the view that super-inertial internal waves are efficient vehicles for TCs to drive remote mixing in the deep ocean (Niwa & Hibiya, 1997; Cuyppers et al., 2013). Furthermore, insight derived from these propagating signals suggests that (ζ, Γ) formulations of fluid dynamics (Névir & Sommer, 2009) can facilitate general analyses of internal wave generation and propagation.

Observations presented here allowed for various complementary analyses of turbulent mixing. First, direct inspection of changes in upper ocean stratification (Figs. 11, 13) helped visualize ML deepening and explain characteristics of the TC wake (Fig. 14). Second, Thorpe scale estimates of ε and κ (Figs. 9b, 10c) help assess the spatial distribution of ocean turbulence, which can then help infer its drivers. Lastly, analysis of observed watermass transformations (Fig. 3) with the diffusive model in (12) and (13) helped constrain the aggregate effect of TC turbulence in upper ocean thermodynamics.

7 Conclusions

Formulating the linear ML dynamics (4)-(6) in terms of ζ and Γ (7)-(9) yields a direct statement of inertial pumping and explains NIW generation behind TCs (Figs. 8, 6). More precisely, this gradient-based view shows that the clockwise steering of currents by $f > 0$ rearranges (u, v) so that ζ evolves into Γ , and Γ into $-\zeta$ (Fig. 4).

Analyzing NIW generation in terms of ζ and Γ instead of the usual (\bar{u}, \bar{v}) helps clarify relations between the ocean response to different types of atmospheric forcing. As the transfer of ζ into the ML by TCs (Fig. 8) allows for immediate generation of NIWs, patterns in $\nabla \times \tau$ and $\nabla \cdot \tau$ associated with other atmospheric phenomena may be studied in a similar fashion. Many questions remain open regarding the partition of wind-work used by mixing, balanced currents, and NIWs under different types of atmospheric forcing (Alford, 2020). Isolating the components (ζ, Γ) of ML flow that contribute to NIW generation thus represents a promising line for future inquiry.

The contribution of winds to the global internal wave budget is often calculated using reanalysis products (Alford, 2001, 2003). However, the spatial resolution of datasets can fail to capture the intensity TC winds (Walsh et al., 2007) and associated upwelling (Vincent et al., 2012). Furthermore, rainfall under TCs can introduce considerable errors to satellite sensors of ocean winds that inform these products (Weissman et al., 2012). Therefore, direct and spatially resolved observations of NIW generation under TCs like those presented here are crucial to better constrain the role of TCs in global budgets of mixing and internal wave energy.

Our analyses indicate that SST cooling beneath Mangkhut was dominated by turbulent entrainment into the ML (Fig. 11), resulting in the formation of an asymmetric cold wake (Fig. 14). Moreover, vertical profiles of density (Fig. 11d) reveal thick (~ 15 m) regions with unstable stratification $\frac{\partial \sigma_\theta}{\partial z} < 0$ that correspond to $\kappa \sim 10^{-1} \text{ m}^2 \text{ s}^{-1}$. Thorpe scale analyses (Fig. 9b, 10c) indicate that mixing rates were greatest near the TC eye where SST cooled the most (Figs. 14). Farther behind in the TC wake, values $\kappa > 10^{-3} \text{ m}^2 \text{ s}^{-1}$ were inferred from observed transformations in T-S properties around $x = 400$ km (Fig. 15). Lastly, near-surface float data detail the effects of turbulence on rain layer formation and destruction (Fig. 13). This is significant given growing awareness about the role of vertical salinity gradients in TC-ocean interactions (Balaguru et al., 2012; Rudzin et al., 2019).

637 **Acknowledgments**

638 Enter acknowledgments, including your data availability statement, here.

639 **References**

- 640 Alford, M. H. (2001). Internal swell generation: The spatial distribution of en-
 641 ergy flux from the wind to mixed layer near-inertial motions. *Journal of Physical*
 642 *Oceanography*, *31*(8), 2359–2368.
- 643 Alford, M. H. (2003). Improved global maps and 54-year history of wind-work on
 644 ocean inertial motions. *Geophysical Research Letters*, *30*(8).
- 645 Alford, M. H. (2020). Revisiting near-inertial wind work: Slab models, relative
 646 stress, and mixed layer deepening. *Journal of Physical Oceanography*, *50*(11),
 647 3141–3156.
- 648 Alford, M. H., & Gregg, M. C. (2001). Near-inertial mixing: Modulation of shear,
 649 strain and microstructure at low latitude. *Journal of Geophysical Research:*
 650 *Oceans*, *106*(C8), 16947–16968.
- 651 Alford, M. H., Gregg, M. C., & Ilyas, M. (1999). Diapycnal mixing in the Banda
 652 Sea: Results of the first microstructure measurements in the Indonesian Through-
 653 flow. *Geophysical Research Letters*, *26*(17), 2741–2744.
- 654 Alford, M. H., MacKinnon, J. A., Simmons, H. L., & Nash, J. D. (2016). Near-
 655 inertial internal gravity waves in the ocean. *Annual review of marine science*, *8*,
 656 95–123.
- 657 Asselin, O., & Young, W. R. (2020, 06). Penetration of Wind-Generated Near-
 658 Inertial Waves into a Turbulent Ocean. *Journal of Physical Oceanography*, *50*(6),
 659 1699-1716. Retrieved from <https://doi.org/10.1175/JPO-D-19-0319.1> doi: 10
 660 .1175/JPO-D-19-0319.1
- 661 Baker, M. A., & Gibson, C. H. (1987). Sampling turbulence in the stratified ocean:
 662 Statistical consequences of strong intermittency. *Journal of Physical Oceanogra-*
 663 *phy*, *17*(10), 1817–1836.
- 664 Balaguru, K., Chang, P., Saravanan, R., Leung, L. R., Xu, Z., Li, M., & Hsieh, J.-S.
 665 (2012). Ocean barrier layers' effect on tropical cyclone intensification. *Proceedings*
 666 *of the National Academy of Sciences*, *109*(36), 14343–14347.
- 667 Bolin, B. (1953). The adjustment of a non-balanced velocity field towards
 668 geostrophic equilibrium in a stratified fluid. *Tellus*, *5*(3), 373–385.
- 669 Cael, B., & Mashayek, A. (2021). Log-skew-normality of ocean turbulence. *Physical*
 670 *Review Letters*, *126*(22), 224502.
- 671 Chang, S. W., & Anthes, R. A. (1978). Numerical simulations of the ocean's nonlin-
 672 ear, baroclinic response to translating hurricanes. *Journal of Physical Oceanogra-*
 673 *phy*, *8*(3), 468–480.
- 674 Chelton, D. B., DeSzoeke, R. A., Schlax, M. G., El Naggar, K., & Siwertz, N.
 675 (1998). Geographical variability of the first baroclinic Rossby radius of defor-
 676 mation. *Journal of Physical Oceanography*, *28*(3), 433–460.
- 677 Chen, S., Cummings, J. A., Schmidt, J. M., Sanabia, E. R., & Jayne, S. R. (2017).
 678 Targeted ocean sampling guidance for tropical cyclones. *Journal of Geophysical*
 679 *Research: Oceans*, *122*(5), 3505–3518.
- 680 Chen, S. S., & Curcic, M. (2016). Ocean surface waves in Hurricane Ike (2008) and
 681 Superstorm Sandy (2012): Coupled model predictions and observations. *Ocean*
 682 *Modelling*, *103*, 161–176.
- 683 Cuyppers, Y., Le Vaillant, X., Bouruet-Aubertot, P., Vialard, J., & McPhaden, M. J.
 684 (2013). Tropical storm-induced near-inertial internal waves during the Cirene
 685 experiment: Energy fluxes and impact on vertical mixing. *Journal of Geophysical*
 686 *Research: Oceans*, *118*(1), 358–380.
- 687 D'Asaro, E. A. (1985). The energy flux from the wind to near-inertial motions in the
 688 surface mixed layer. *Journal of Physical Oceanography*, *15*(8), 1043–1059.

- 689 D’Asaro, E. A. (1989). The decay of wind-forced mixed layer inertial oscillations due
690 to the β effect. *Journal of Geophysical Research: Oceans*, *94*(C2), 2045–2056.
- 691 D’Asaro, E. A. (2003). The ocean boundary layer below Hurricane Dennis. *Journal*
692 *of Physical Oceanography*, *33*(3), 561–579.
- 693 D’Asaro, E. A., Sanford, T. B., Niiler, P. P., & Terrill, E. J. (2007). Cold wake of
694 hurricane Frances. *Geophysical Research Letters*, *34*(15).
- 695 Davis, R., Sherman, J., & Dufour, J. (2001). Profiling ALACEs and other advances
696 in autonomous subsurface floats. *Journal of atmospheric and oceanic technology*,
697 *18*(6), 982–993.
- 698 Davis, R. E. (1985). Objective mapping by least squares fitting. *Journal of Geophys-*
699 *ical Research: Oceans*, *90*(C3), 4773–4777.
- 700 Ekman, V. W. (1905). On the influence of the earth’s rotation on ocean-currents.
- 701 Emanuel, K. (2001). Contribution of tropical cyclones to meridional heat transport
702 by the oceans. *Journal of Geophysical Research: Atmospheres*, *106*(D14), 14771–
703 14781.
- 704 Emanuel, K. (2005). Increasing destructiveness of tropical cyclones over the past 30
705 years. *Nature*, *436*(7051), 686–688.
- 706 Emanuel, K. A. (1999). Thermodynamic control of hurricane intensity. *Nature*,
707 *401*(6754), 665–669.
- 708 Geisler, J. E. (1970). Linear theory of the response of a two layer ocean to a moving
709 hurricane. *Geophysical and Astrophysical Fluid Dynamics*, *1*(1-2), 249–272.
- 710 Gill, A. (1984). On the behavior of internal waves in the wakes of storms. *Journal of*
711 *Physical Oceanography*, *14*(7), 1129–1151.
- 712 Glenn, S., Miles, T., Seroka, G., Xu, Y., Forney, R., Yu, F., . . . Kohut, J. (2016).
713 Stratified coastal ocean interactions with tropical cyclones. *Nature communica-*
714 *tions*, *7*(1), 1–10.
- 715 Guan, S., Zhao, W., Huthnance, J., Tian, J., & Wang, J. (2014). Observed upper
716 ocean response to typhoon Megi (2010) in the Northern South China Sea. *Journal*
717 *of Geophysical Research: Oceans*, *119*(5), 3134–3157.
- 718 Hautala, S. L., Reid, J. L., & Bray, N. (1996). The distribution and mixing of
719 Pacific water masses in the Indonesian Seas. *Journal of Geophysical Research:*
720 *Oceans*, *101*(C5), 12375–12389.
- 721 Huffman, G. J., Bolvin, D. T., Braithwaite, D., Hsu, K., Joyce, R., Xie, P., & Yoo,
722 S.-H. (2015). NASA global precipitation measurement (GPM) integrated multi-
723 satellite retrievals for GPM (IMERG). *Algorithm Theoretical Basis Document*
724 *(ATBD) Version, 4*, 26.
- 725 Jacob, S. D., Shay, L. K., Mariano, A. J., & Black, P. G. (2000). The 3D oceanic
726 mixed layer response to Hurricane Gilbert. *Journal of Physical Oceanography*,
727 *30*(6), 1407–1429.
- 728 Johnston, T. M. S., Chaudhuri, D., Mathur, M., Rudnick, D. L., Sengupta, D., Sim-
729 mons, H. L., . . . Venkatesan, R. (2016). Decay mechanisms of near-inertial mixed
730 layer oscillations in the Bay of Bengal. *Oceanography*, *29*(2), 180–191.
- 731 Johnston, T. M. S., & Rudnick, D. L. (2009). Observations of the transition layer.
732 *Journal of physical oceanography*, *39*(3), 780–797.
- 733 Johnston, T. M. S., Rudnick, D. L., Brizuela, N., & Moum, J. N. (2020). Advection
734 by the North Equatorial Current of a cold wake due to multiple typhoons in the
735 western Pacific: Measurements from a profiling float array. *Journal of Geophysical*
736 *Research: Oceans*, *125*(4), e2019JC015534.
- 737 Johnston, T. M. S., Wang, S., Lee, C.-Y., Moum, J. N., Rudnick, D. L., & Sobel, A.
738 (2021). Near-inertial wave propagation in the wake of Super Typhoon Mangkhut:
739 Measurements from a profiling float array. *Journal of Geophysical Research:*
740 *Oceans*, e2020JC016749.
- 741 Kundu, P. K., & Thomson, R. E. (1985). Inertial oscillations due to a moving front.
742 *Journal of physical oceanography*, *15*(8), 1076–1084.

- 743 Kunze, E. (1985). Near-inertial wave propagation in geostrophic shear. *Journal of*
744 *Physical Oceanography*, 15(5), 544–565.
- 745 Le Traon, P., Nadal, F., & Ducet, N. (1998). An improved mapping method of mul-
746 tisatellite altimeter data. *Journal of atmospheric and oceanic technology*, 15(2),
747 522–534.
- 748 Mei, W., Primeau, F., McWilliams, J. C., & Pasquero, C. (2013). Sea surface height
749 evidence for long-term warming effects of tropical cyclones on the ocean. *Proceed-*
750 *ings of the National Academy of Sciences*, 110(38), 15207–15210.
- 751 Moum, J., Farmer, D., Smyth, W., Armi, L., & Vagle, S. (2003). Structure and gen-
752 eration of turbulence at interfaces strained by internal solitary waves propagating
753 shoreward over the continental shelf. *Journal of Physical Oceanography*, 33(10),
754 2093–2112.
- 755 Névir, P., & Sommer, M. (2009). Energy–vorticity theory of ideal fluid mechanics.
756 *Journal of the atmospheric sciences*, 66(7), 2073–2084.
- 757 Nilsson, J. (1995, 04). Energy flux from traveling hurricanes to the oceanic internal
758 wave field. *Journal of Physical Oceanography*, 25(4), 558–573.
- 759 Niwa, Y., & Hibiya, T. (1997). Nonlinear processes of energy transfer from traveling
760 hurricanes to the deep ocean internal wave field. *Journal of Geophysical Research:*
761 *Oceans*, 102(C6), 12469–12477.
- 762 Pearson, B., & Fox-Kemper, B. (2018). Log-normal turbulence dissipation in global
763 ocean models. *Physical review letters*, 120(9), 094501.
- 764 Pollard, R. T. (1970). On the generation by winds of inertial waves in the ocean. In
765 *Deep sea research and oceanographic abstracts* (Vol. 17, pp. 795–812).
- 766 Pollard, R. T., & Millard Jr, R. (1970). Comparison between observed and simu-
767 lated wind-generated inertial oscillations. In *Deep sea research and oceanographic*
768 *abstracts* (Vol. 17, pp. 813–821).
- 769 Price, J. F. (1981). Upper ocean response to a hurricane. *Journal of Physical*
770 *Oceanography*, 11(2), 153–175.
- 771 Price, J. F. (1983). Internal wave wake of a moving storm. Part I. Scales, energy
772 budget and observations. *Journal of Physical Oceanography*, 13(6), 949–965.
- 773 Rossby, C.-G. (1938). On the mutual adjustment of pressure and velocity distribu-
774 tions in certain simple current systems, II. *J. mar. Res.*, 1(3), 239–263.
- 775 Rudzin, J. E., Shay, L. K., & Jaimes de la Cruz, B. (2019). The impact of the
776 Amazon–Orinoco River plume on enthalpy flux and air–sea interaction within
777 Caribbean Sea tropical cyclones. *Monthly Weather Review*, 147(3), 931–950.
- 778 Sanford, T. B., Price, J. F., & Garton, J. B. (2011). Upper-ocean response to Hur-
779 ricane Frances (2004) observed by profiling EM-APEX floats. *Journal of Physical*
780 *Oceanography*, 41(6), 1041–1056.
- 781 Shay, L. K., & Chang, S. W. (1997). Free surface effects on the near-inertial ocean
782 current response to a hurricane: A revisit. *Journal of Physical Oceanography*,
783 27(1), 23–39.
- 784 Shay, L. K., Elsberry, R. L., & Black, P. G. (1989). Vertical structure of the ocean
785 current response to a hurricane. *Journal of Physical Oceanography*, 19(5), 649–
786 669.
- 787 Skamarock, W. C., Klemp, J. B., Dudhia, J., Gill, D. O., Barker, D. M., Wang, W.,
788 & Powers, J. G. (2008). A description of the Advanced Research WRF version 3.
789 NCAR Technical note-475+ STR.
- 790 Sriver, R. L., & Huber, M. (2007). Observational evidence for an ocean heat pump
791 induced by tropical cyclones. *Nature*, 447(7144), 577–580.
- 792 Thompson, A. F., Gille, S. T., MacKinnon, J. A., & Sprintall, J. (2007). Spatial
793 and temporal patterns of small-scale mixing in Drake Passage. *Journal of Physical*
794 *Oceanography*, 37(3), 572–592.
- 795 Thompson, E. J., Moum, J. N., Fairall, C. W., & Rutledge, S. A. (2019). Wind
796 limits on rain layers and diurnal warm layers. *Journal of Geophysical Research:*

- 797 *Oceans*, 124(2), 897–924.
- 798 Thorpe, S. (1973). Experiments on instability and turbulence in a stratified shear
799 flow. *Journal of Fluid Mechanics*, 61(4), 731–751.
- 800 Thorpe, S. A. (1977). Turbulence and mixing in a Scottish loch. *Philosophical*
801 *Transactions of the Royal Society of London. Series A, Mathematical and Physical*
802 *Sciences*, 286(1334), 125–181.
- 803 Veronis, G. (1956). Partition of energy between geostrophic and non-geostrophic
804 oceanic motions. *Deep Sea Research (1953)*, 3(3), 157–177.
- 805 Vincent, E. M., Lengaigne, M., Madec, G., Vialard, J., Samson, G., Jourdain, N. C.,
806 ... Jullien, S. (2012). Processes setting the characteristics of sea surface cooling
807 induced by tropical cyclones. *Journal of Geophysical Research: Oceans*, 117(C2).
- 808 Wallcraft, A., Metzger, E., & Carroll, S. (2009). *Software design description for*
809 *the hybrid coordinate ocean model (HYCOM), Version 2.2* (Tech. Rep.). Naval Re-
810 search Lan Stennis Space Center MS Oceanography Div.
- 811 Walsh, K., Fiorino, M., Landsea, C., & McInnes, K. (2007). Objectively determined
812 resolution-dependent threshold criteria for the detection of tropical cyclones in
813 climate models and reanalyses. *Journal of climate*, 20(10), 2307–2314.
- 814 Wamsley, L. (2018, Sep). Dozens more feared dead in the philippines after typhoon
815 triggers mudslide. *National Public Radio*. Retrieved from [https://www.npr.org/](https://www.npr.org/2018/09/17/648866035/dozens-more-feared-dead-in-the-philippines-after-typhoon-triggers-mudslide)
816 [2018/09/17/648866035/dozens-more-feared-dead-in-the-philippines-after](https://www.npr.org/2018/09/17/648866035/dozens-more-feared-dead-in-the-philippines-after-typhoon-triggers-mudslide)
817 [-typhoon-triggers-mudslide](https://www.npr.org/2018/09/17/648866035/dozens-more-feared-dead-in-the-philippines-after-typhoon-triggers-mudslide)
- 818 Weissman, D., Stiles, B., Hristova-Veleva, S., Long, D., Smith, D., Hilburn, K., &
819 Jones, W. (2012). Challenges to satellite sensors of ocean winds: Addressing
820 precipitation effects. *Journal of Atmospheric and Oceanic Technology*, 29(3),
821 356–374.
- 822 Zedler, S. E. (2009). Simulations of the ocean response to a hurricane: Nonlinear
823 processes. *Journal of Physical Oceanography*, 39(10), 2618–2634.
- 824 Zweers, N., Makin, V., De Vries, J., & Burgers, G. (2010). A sea drag relation for
825 hurricane wind speeds. *Geophysical Research Letters*, 37(21).